学位論文

Study on Epitaxial Perovskite Li-ion Conducting Thin Films: Strain-controlled Ionic Conduction and Heterostructure

(ペロブスカイト型Liイオン伝導体エピタキシャル薄膜の研究：

歪制御イオン伝導とヘテロ構造)

平成２７年７月博士（理学）申請

東京大学大学院理学系研究科

化学専攻

韋 嵘

Study on Epitaxial Perovskite Li-ion Conducting Thin Films: Strain-controlled Ionic Conduction and Heterostructure

by

Jie Wei

Department of Chemistry

Graduate School of Science

The University of Tokyo

July, 2015

Abstract

Li-ion conductors acted as solid electrolyte have attracted great attentions in the researches of all solid state Li-ion batteries. Among the known Li-ion conductors, lithium lanthanum titanate $Li_{3x}La_{2/3-x}TiO_3$ (LLT, $0.05 < x < 0.167$) with A-site vacant perovskite structure shows the ionic conductivity up to 1 mS/cm at room temperature, which is comparable to those in conventional organic solvent electrolytes. Since grain boundaries significantly suppress the Li ionic conductivity in bulk LLT specimens, single crystal sample is required, but difficult to obtain in bulk study. The demand for obtaining single crystal has stimulated epitaxial thin film study to fabricate highly crystalline LLT. Recently, epitaxial thin film growth of LLT by pulsed laser deposition (PLD) attracted many interests to prepare single crystal specimens. However, in these researches, stoichiometric LLT was hard to obtained due to the Li-loss in fabrication process, thus it strangles further property investigation.

In this dissertation, highly crystalline epitaxial LLT thin film with stoichiometric composition was fabricated on various perovskite substrates. Laser fluence was discovered as the key factor related to the Li-loss and was varied to control Li-composition precisely. Also, Li-rich LLT target was used in PLD process in order to compensate the Li-loss observed in the previous experiments. By optimizing the laser fluence in addition to other PLD parameters, highly crystalline LLT thin film with stoichiometric composition was obtained, enabling the measurement of intrinsically high ionic conductivity. The ionic conductivity in epitaxial thin films was comparable to that in polycrystalline specimens without showing grain-boundary conductivity which suppressed the total ionic conductivity in polycrystalline bulk study.

Strain-controlled effects on LLT crystal structure were investigated on LLT epitaxial thin films. By altering the substrates with different in-plane lattice constants, orientation

of LLT thin films was controlled as *a*-axis oriented with two kinds of in-plane domains perpendicular to each other under tensile strain, while *c*-axis oriented thin films were obtained with single domain under compressive strain.

Strain-controlled ionic conductivity of LLT was also investigated in LLT thin film on orthorhombic $NdGaO_3$ (110) substrate due to the anisotropic distortion of in-plane LLT lattice. In LLT epitaxial thin films, the ionic conductivity decreased with a increasing activation energy under an increasing compressive strain. The more contracted bottleneck generated from larger compressive strain enhanced the difficulty of Li-ion hopping. Different from the similar tendency showing in bulk research, the strain-controlled effects in epitaxial thin films are stable in the atmospheric condition. This research proved that epitaxial strain is very effective in controlling Li ionic conduction.

In addition, LLT heteroepitaxial structures were formed on $La_{0.6}Sr_{0.4}MnO_3$ (LSMO) bottom electrode layer as a preliminary study toward all solid state epitaxial Li-ion batteries. The interface between LLT and LSMO was studied in detail by X-ray reflectometry. LLT/LSMO interface was found to be rough as well as the interface between LLT and LSAT/$SrTiO_3$ substrates, probably due to Sr-La intermixing.

In conclusion, highly crystalline epitaxial LLT thin films with stoichiometric composition were successfully fabricated. The researches on LLT thin films indicated that it is possible to control the crystal structure and ionic conductivity by applying epitaxial strain. The investigations on heterostructure, which was formed by LLT thin film on LSMO bottom electrode, indicated the complicated interface structures and revealed the possibility to construct epitaxial battery structure by thin film growth. The strain-controllable LLT thin film as well as its heterostructure provides a deeper prospect to understand the intrinsic properties of LLT, leading to the application of all solid epitaxial device.

Acknowledgement

I want to give my great thanks to my supervisor Prof. Tetsuya Hasegawa, for all the academic guidance and encouragement. He provided me the opportunity to study in the University of Tokyo and the wonderful experimental environments. He has encouraged, supported and inspired me to investigate the infinite possibilities. Whenever I met the difficulties and hesitations, he was always more generous than sharing the knowledge.

I am very appreciated to work with Prof. Tomoteru Fukumura. His deep insight on solid state chemistry as well as patience and enthusiasm supported me through every research experience. He always encouraged me to challenge new ideas and fields without fearing about failure. With his supports, I acquired many academic skills as well as the thinking mode to bring out new ideas.

I would also give my thanks to Prof. Yasushi Hirose for his thoughtful advices in my experiments as well as the support in experimental techniques. I also owe this dissertation to Dr. Akira Chikamatsu, Dr. Hideyuki Kamisaka and Mr. Shoichiro Nakao for their kindness in sharing their experience to promote my research.

I would like to appreciate Dr. Daisuke Ogawa for his technical help in electrode fabrication and ionic conductivity measurement, in addition to his important contribution on this dissertation work. I would like to appreciate Prof. Atsushi Fujimori as the vice-supervisor in ALPS program for his fruitful discussion from the point view of a physicist.

I am deeply grateful to Shungo Kojima, Shun Inoue, Thantip S. Krasienapibal, Ryosuke Sei, Mayuko Oka, Ken'ichi Kaminaga, Kyouhei Yamatake, Yutaka Uchida, Dai Kutsuzawa, Shunsuke Shibata as the members of the same project in daily discussion and supports in experiments. I also thanks to all the members in Hasegawa laboratory: Dr. Sohei Okazaki, Dr. Chang Yang, Dr. Youngok Park, Dr. Anri Watanabe, Tsukasa Katayama, Atsuchi Suzuki, Il Jeon, Xi Shen, Kazuki Aizawa, Kenta Shimamoto, Tomoya

Onozuka, Ryosuke Takagi, Kaori Kurita, Jumpei Takahashi, Masahito Sano, Vitchaphol Motaneeyachart, Takanori Yamazaki, Keisuke Kawahara, Yuji Kurauchi, Fahd S. Khan, Ryota Kantake, Keisuke Yamada, Naoki Kashiwa, Miho Otaki. I would also thank the secretaries, Ms. Mie Umino, Ms. Miki Komazawa, Ms. Mayumi Kikuchi and Ms. Aya Imoji for their supports.

I would give special thanks to Japanese government for providing MEXT scholarship as financial support in the past five years. I also thanks ALPS program and JFE Mineral for the opportunity of internship.

Finally, I would like to express my gratefulness to my family for their devotion and supports all the time.

Contents

1 General introduction

1.1 Lithium-ion battery

Rechargeable batteries, also known as secondary batteries, have become key components of modern electronic industry due to the explosively increasing needs of portable entertainment devices in mobile society. Among all kinds of rechargeable batteries, Li-ion battery (LIB) is one of the most popular type because of its high energy density, lack of memory effect and slow rate of charge loss when not in use. It is also more environmental friendly and safer than its precursors such as lead acid batteries which are commonly used in traditional vehicles. Therefore, it has become a commercially available candidate of replacement in electronic vehicles industry. However, compared with the spectacular advances in energy consuming technologies such as computers and mobile devices, technology of batteries still cannot keep the pace and is always criticized for its slow development. This requirement has driven a large number of researches in this field to develop batteries with higher energy density, faster charge rate and more charge cycles with less safety concern.

Figure 1.1 shows a representative structure of commercial LIBs. The commercial LIBs are generally based on Li-intercalated metal oxide cathodes and graphite anodes. When charging LIBs, Li^+ will deintercalate from the cathode and deposit on the anode side. On the other hand, when energy is extracted from LIBs during discharging, Li^+ moves to the cathode side from the anode. Similar to traditional primary batteries, LIBs contain cathode, anode and electrolyte as their components. On the other hand, LIBs utilize Li-ions, not electrons as charge transfer species, making the unique requirement of material selections due to the high electropositivity and instability of Li compounds. By reviewing the history of LIBs technology, one can find the present status of research

and challenges for the future.

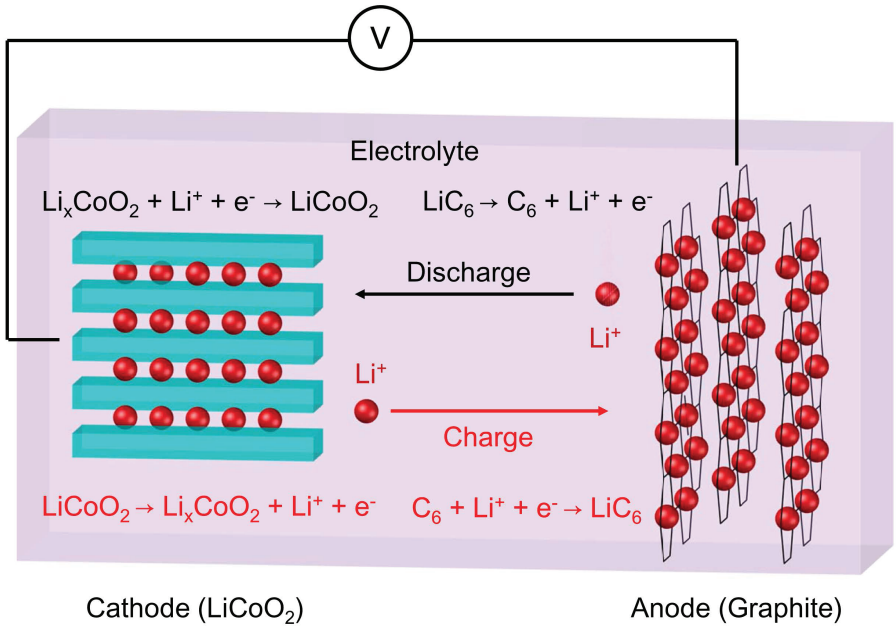

Figure 1.1 Schematic structure of commercial LIBs

Experiments based on lithium metal anodes began in the age of early 20th century, when G. N. Lewis proposed his theory about acid and alkali. The motivation to apply Li metal as anode was driven by the fact that Li is the lightest metal with high electropositivity so that the theoretical energy density is rather high. However, it was hard to form a rechargeable cell due to lack of suitable cathode until Li intercalation into layered transition metal dichalcogenides was discovered in 1970s [1].

The first practical LIBs structure was proposed by M. S. Whittingham in 1976 at Exxon with a layered TiS_2 cathode and Li metal anode to achieve a cell voltage of 2.5 V, although they suffered from safety issues due to the highly reactive anode [2, 3, 4]. In 1979, J. Goodenough demonstrated a rechargeable LIB using layered $LiCoO_2$ as cathode and Li metal anode to perform a cell voltage of 4 V [5], whose layered metal oxide cathodes became the most commonly used electrode in LIBs industry till now. In 1980, R. Yazami proposed the first prototype of graphite anode for LIBs through proving the

reversible intercalation of Li in graphite by electrochemical reaction [6]. In 1985, A. Yoshino, Asahi Kasei Co. claimed a patent about the prototype of LIBs, using metal oxides as cathode and carbonaceous materials as anode with a separator and nonaqueous electrolytes [7]. In 1991, Sony and Asahi Kasei released the first commercial LIB product, representing the birth of LIB industry [8]. Since LIBs were born, most of the researches focused on the improvement of capacity and charge-discharge rate by developing new cathode and anode materials. During the past two decades, the energy density of LIBs has increased by three times while the cost has dropped to 1/30 of the original product [9].

1.2 Liquid electrolytes

Compared with the significant advances in electrodes, improvement of electrolytes seems not notable. Until now, most of the commercial LIB products are still using the same type of electrolytes as twenty years ago, which are based on lithium salts and organic alkyl carbonates solvents. A standard type of electrolyte is lithium hexafluorophosphate ($LiPF_6$) dissolved in ethylene carbonate (EC) mixed with ethyl methyl carbonate (EMC), diethyl carbonate (DEC) or/and dimethyl carbonate (DMC) [10, 11]. These electrolytes have high ionic conductivity up to 10 mS/cm at room temperature, high anodic stability due to the wide potential range vs. Li/Li^+ and low fabrication cost. However, disadvantages of these electrolyte solutions are also obvious for LIBs, which are [11, 12]:

- Low stability against temperature. The solutions freeze at low temperature and the ionic conductivity drops significantly, while at elevating temperature over 60°C, the vapor pressure of the solvent increases drastically with explosion risk.
- Not compatible for shaped and light LIBs. As they are liquid, most of the LIBs products have to be covered by metal shells to seal up the electrolytes. This

increases the weight of battery and is not flexible for varied shapes and sizes in mobile and micro devices.

- Decomposition of salts. It is believed that $LiPF_6$ can decompose into LiF and PF_5 by a reversible process (Equation (1.1)). An unavoidable trace amount of water brought from fabrication process will easily react with the strong Lewis acid PF_5 as represented by the following mechanism (Equation (1.2)) [13]. As a result, insolvable LiF deposits on surface of electrodes, blocking the Li diffusion path by passivation layers, while HF causes corrosion of cathode materials. Also, HF may react with ROLi and $ROCO_2Li$ species at the electrode surface, forming LiF and reducing the total capacity in the battery.

$$LiPF_6 \rightleftharpoons LiF\downarrow + PF_5 \tag{1.1}$$

$$PF_5 + H_2O \longrightarrow PF_3O + 2HF \tag{1.2}$$

- Decomposition of solution. K. Kumai et al. proposed the following mechanism (Equations (1.3) to (1.6)) for solution decomposition by analyzing the gas generated from LIBs using GC/MS [14]. It is believed that the generation of these flammable alkyl gases causes most of the explosion accidents. Because of the safety concern of explosion, logistics of LIBs requires licenses and high cost to prevent accidents in distribution network.

$$ROCO_2R + Li^+ + e^- \longrightarrow ROCO_2Li\downarrow + R\cdot \tag{1.3}$$

$$ROCO_2Li + Li^+ + e^- \longrightarrow Li_2CO_3\downarrow + R\cdot \tag{1.4}$$

$$R\cdot + H_2 \longrightarrow R{-}H + H\cdot \tag{1.5}$$

$$R\cdot + R\cdot \longrightarrow R{-}R\uparrow \tag{1.6}$$

In order to solve these problemes, stable solid state electrolytes are required. One of the commercialized approach is to solidify the liquid electrolytes by mixing with poly-

mers [15, 16]. However, inevitable dissolution of those solidified species is still a practical problem.

1.3 Inorganic solid electrolytes

Inorganic solid lithium ion electrolytes are considered to take the place of organic solvents and polymer-based ones, due to their high thermal stability at a wide temperature range and inflammable property related to the safety concern. Moreover, LIBs using inorganic solid electrolytes can be more compact by using multiple stacking structure (Figure 1.2) [17], leading to higher practical energy density. Solid electrolytes are also flexible to shape and size, supporting the micro battery in micro devices in chip industry and medical applications. To realize the potential applications, inorganic solid electrolyte materials require various functional properties including [17, 18]:

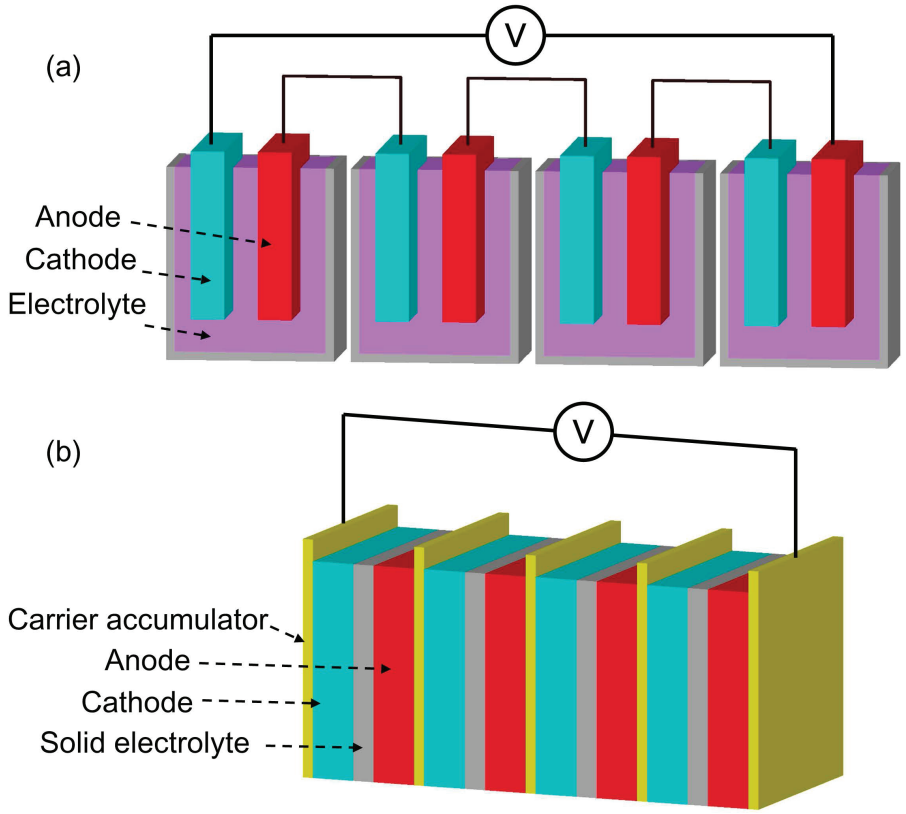

Figure 1.2 Comparison of multiple stacking LIBs using (a) liquid electrolytes and (b) solid electrolytes. [17]

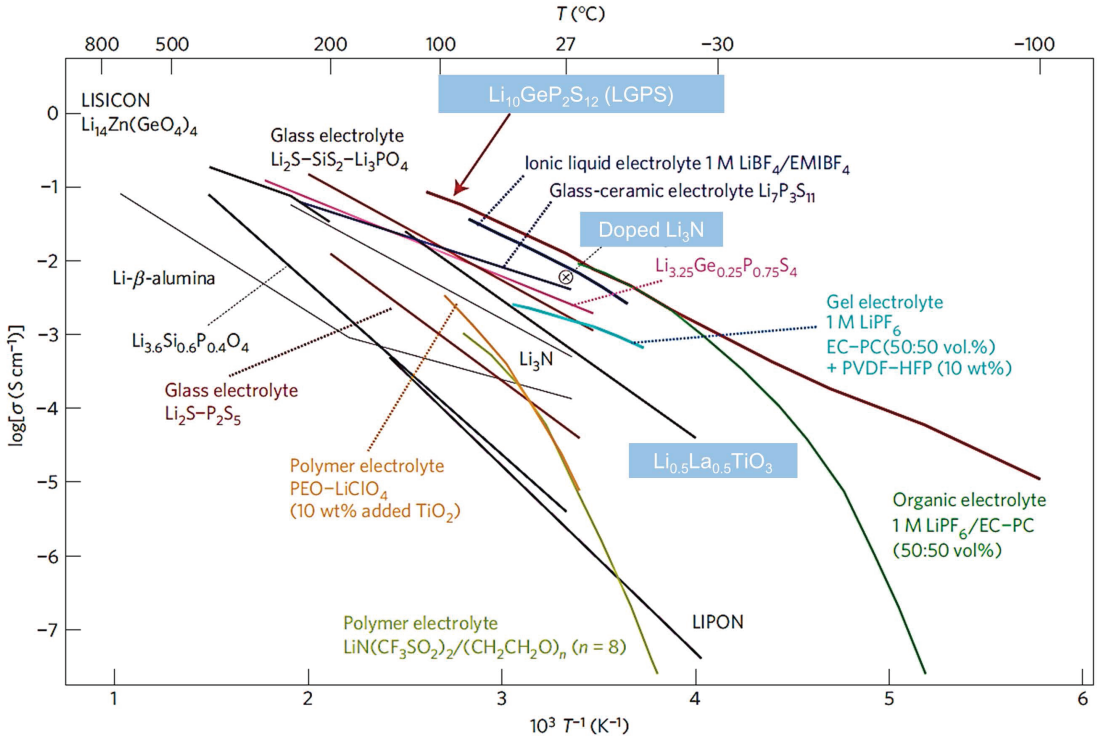

Figure 1.3 Ionic conductivity of various solid electrolytes, together with liquid electrolytes solutions, polymer electrolyte and gel electrolytes. Reprinted by permission from Macmillan Publishers Ltd: *Nature Materials* [19], Copyright 2011.

- High total ionic conductivity up to 1 mS/cm.
- Chemical stability against reactions at electrode-electrolyte interface.
- Low charge-transfer resistance at solid-state electrode-electrolyte interface.
- Low cost fabrication method.

To achieve these goals, a large number of researches have been studied in the past few decades for discovering new materials. Various types of inorganic materials from amorphous to crystalline, from oxides to non-oxides, have been investigated, including lithium doped β-alumina (Li-β-Al_2O_3) [20], Li_3N [21, 22], phosphates with sodium super ionic conductor structure (NASICON-type) [23], lithium super ionic conductor type oxides (LISICON-type) [24], glass electrolyte (LiPON [25], Li_2S-P_2S_5[26] and Li_2S-SiS_2-Li_3PO_4[27]), Thio-LISICON $Li_{3.25}Ge_{0.25}P_{0.25}S_4$ [28], perovskite $Li_{3x}La_{2/3-x}TiO_3$

(LLT) [29], garnet-type $Li_5La_3M_2O_{12}$ (M = Nb, Ta) [30], $Li_{10}GeP_2S_{12}$ (LGPS) [19] and so on. Among them, LLT, Li_3N and LGPS exhibit high ionic conductivity as shown in Figure 1.3. Although LGPS shows the highest room temperature ionic conductivity up to 10 mS/cm which is comparable to $LiPF_6$ solution electrolytes, it suffers great drawback from the sulfide-oxide dead layer at the interface between cathode and electrolyte [31] as well as the instability against moisture and reduction [32]. Li_3N, another material with high ionic conductivity up to 5 mS/cm, has a low decomposition potential vs Li/Li^+ (0.44 V) [22]. Therefore, its application to all-solid-state battery should be quite limited to low voltage cell.

1.4 Lithium lanthanum titanates

As mentioned above, perovskite type lithium lanthanum titanates $Li_{3x}La_{2/3-x}TiO_3$ (LLT, $0 < x < 0.16$) has high ionic conductivity up to the order of 1 mS/cm under room temperature. Compared with other inorganic solid state electrolytes, it is stable over a wide range of temperature and is also available as a high voltage cathode due to its high electrochemical stability.

1.4.1 Bulk study

LLT was first fabricated by Y. Inaguma et al. in 1993 by solid state reaction through sintering a stoichiometric mixture of Li_2CO_3, La_2O_3 and TiO_2 [29]. LLT has an ABO_3 perovskite structure as shown in Figure 1.4. The A-site in perovskite structure is not fully occupied by Li^+ and La^{3+}, but contains a certain amount of vacancies, allowing hopping of a Li-ion to its neighbour A-site through a bottleneck formed by four O-ions.

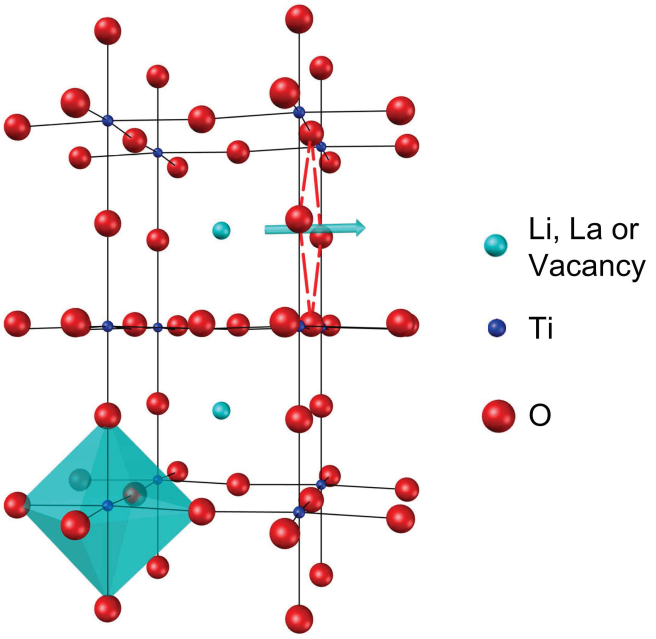

Figure 1.4 Perovskite structure of LLT. Reprint with permissions from "Epitaxial Strain-Controlled Ionic Conductivity in Li-Ion Solid Electrolyte $Li_{0.33}La_{0.56}TiO_3$ Thin Films", Jie Wei, Daisuke Ogawa, Tomoteru Fukumura, Yasushi Hirose and Tetsuya Hasegawa, *Cryst. Growth Des.,* **2015,** *15*(5), 2187-2191. Copyright 2015 American Chemical Society.

LLT has a mixture of two phases, high-temperature A-site disordered α-LLT and low-temperature A-site ordered β-LLT, featured by the distribution of Li^+ and La^{3+}, as shown in Figure 1.5. Reversible phase transition was proved by Y. Harada et al. by controlled cooling process of bulk samples [33, 34]. They claimed that quenching resulted in A-site disordered cubic LLT, in which A-site cations were randomly arranged, while slow cooling process introduced A-site ordered tetragonal phase. T. Okumura et al. studied local structures of the two phases by extended X-ray absorption fine structure [35]. They believed that the A-site ordering changes the inter-atomic Columbic repulsion force between lithium and surrounding ions, which generates the difference of ionic migration behavior between two kinds of LLT.

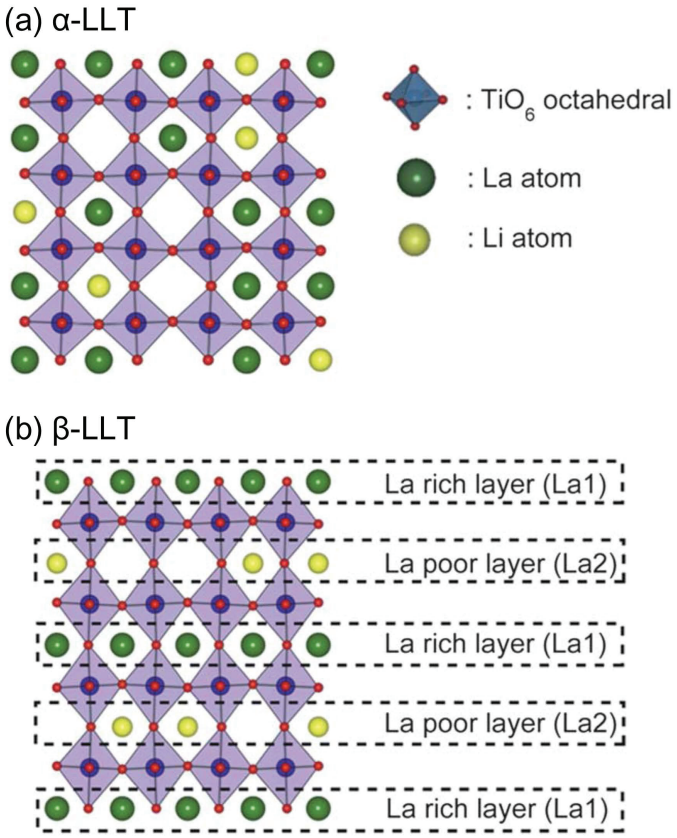

Figure 1.5 Structure of (a) A-site disordered α-LLT and (b) A-site ordered β-LLT. Reproduced from Ref. [35] with permission of The Royal Society of Chemistry.

It is believed that the ionic conductivity of LLT is mainly governed by carrier concentration and bottleneck size. As for the former, Y. Inaguma et al. studied the influence of carrier concentration by varying x in $Li_{3x}La_{2/3-x}TiO_3$ and discovered that ionic conductivity is a parabolic function of x with a maximum at $x = 0.11$ ($Li_{0.33}La_{0.56}TiO_3$), as shown in Figure 1.6 [36]. They proposed an empirical equation to describe this relation as Equation (1.7).

$$\begin{aligned} \sigma &\propto m(1-m)(n'-n_c)^2 \\ &= \frac{3x(1/3-2x)}{(1/3+x)^2}\left[(\frac{1}{3}+x)-n_c\right]^2 \end{aligned} \tag{1.7}$$

where σ is the ionic conductivity, n' is the total concentration of lithium and vacancy, m is the ratio of lithium concentration to n', n_c is a constant equals to 0.3117 for simple cubic lattice.

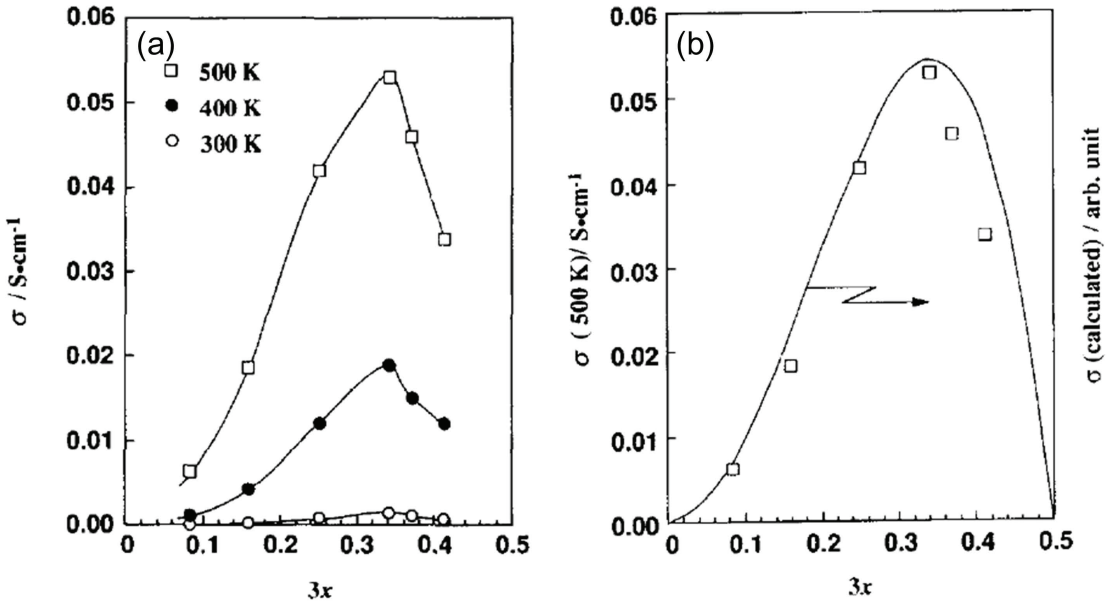

Figure 1.6 Ionic conductivity of LLT (a) as a function of x at various temperatures and (b) comparison to calculation by Equation (1.7). Reprinted from Ref. [36], Copyright 1996, with permission from Elsevier.

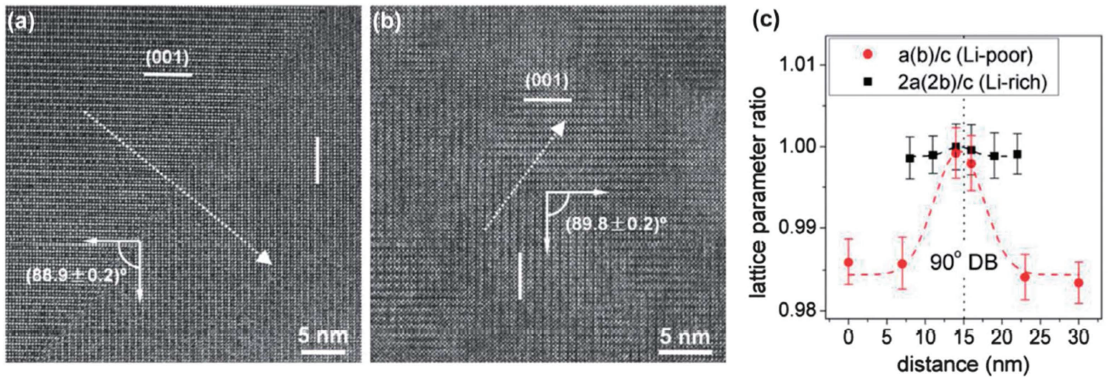

Figure 1.7 High resolution transmission electron microscopy images for the (a) Li-poor $Li_{0.16}La_{0.62}TiO_3$ and (b) Li-rich $Li_{0.33}La_{0.56}TiO_3$ polycrystalline bulk samples. (c) Lattice parameter ratio across 90° domain boundaries along the direction of arrows shown in (a) and (b), respectively. Reproduced from Ref. [37] with permission of The Royal Society of Chemistry.

It is also known that the concentration of Li does not only affect the ionic conductivity. Several neutron diffraction studies have indicated that the occupancies of La and Li in Li-rich LLT [38] were different from those in Li-poor LLT [39], resulting in varied Li-diffusion behavior [40]. X. Gao et al. studied the microstructures of Li-rich and Li-poor

LLT by scanning transmission electron microscopy [37, 41] and observed more distorted domain boundaries with angle of 90° in Li-poor LLT samples (Figure 1.7), suppressing the migration mobility of Li-ions.

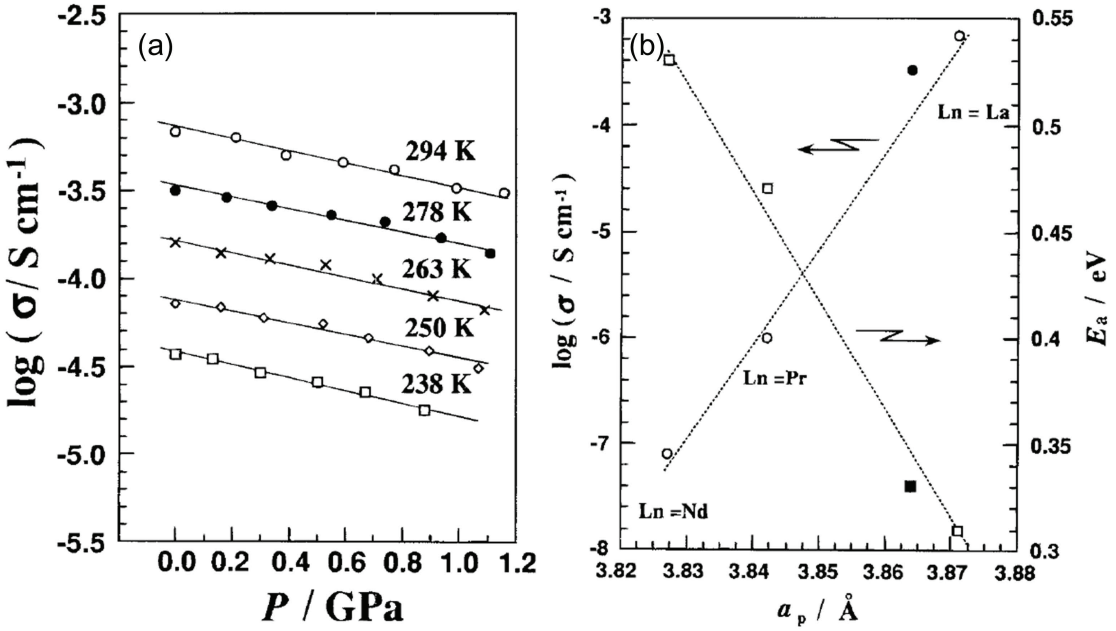

Figure 1.8 (a) Pressure dependence of bulk ionic conductivity in polycrystalline $Li_{0.35}La_{0.52}TiO_{2.96}$. (b) Ionic conductivities (open circles) and activation energies (open square) of $Li_{0.34}Ln_{0.56}TiO_3$ (Ln = La, Pr, Nd) in relation with their lattice parameters a_p at room temperature and atmospheric pressure. Solid circle and square show the ionic conductivity and activation energy of LLT under 1.0 GPa, respectively. Reprinted with permission from [42]. Copyright 1995, The Electrochemical Society.

As for the bottleneck, Y. Inaguma et al. studied the effect of compressive strain on ionic conductivity in LLT through hydrostatic pressure and replacement of La by Ln (Ln = Pr and Nd) with smaller ionic radius (Figure 1.8) [42]. By applying hydrostatic pressure up to 1.2 GPa, ionic conductivity of LLT dropped with an increasing activation energy. Similar tendency was observed by replacing La with Pr and Nd, where the LLT lattice shrank due to the smaller ionic radius of A-site cations. From their results, it was concluded that both mechanical and chemical compressive strains lead to low ionic conductivity and high activation energy in LLT. Furthermore, they calculated the activation volume for ionic conductivity and it was consistent with the activation volume derived

from the four-oxygen bottleneck hopping mechanism, indicating that bottleneck size was the key factor affecting the ionic conductivity. Since tensile strain was not easy to apply on bulk samples directly, T. Okumura et al. used F-doping on anion site to expand the bottleneck, resulting in improvement of ionic conductivity [43, 44].

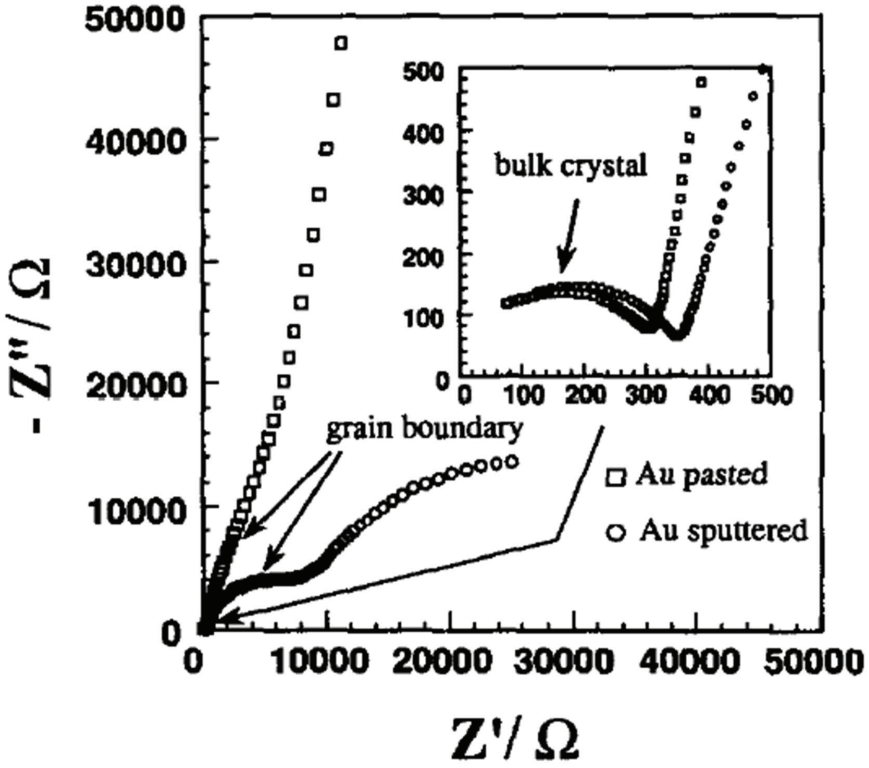

Figure 1.9 Cole-Cole plots for LLT with Au electrodes measured at 300 K. Reprinted from Ref. [29] Copyright 1993, with permission from Elsevier.

Although LLT has attracted great interest for its high bulk ionic conductivity, its disadvantage is also obvious: low grain boundary ionic conductivity. Figure 1.9 shows typical complex impedance Cole-Cole plots for polycrystalline sample [29]. One can find that the resistance of grain boundary in large semicircle contributed too much to the total ionic conductivity. Compared with the bulk ionic conductivity up to the order of 1 mS/cm, the grain boundary ionic conductivity is only of the order of 10^{-2} mS/cm, two orders lower than that of bulk. To solve this problem, single crystal LLT is required. Y. Inaguma et al. attempted to apply floating zone method to fabricate single crystal LLT

[45], but the obtained crystal contained domains with an average size of 100 nm [46]. Till now, there is still no other reports on bulk single crystal LLT, demonstrating the difficulty of single crystal fabrication.

1.4.2 Thin film study

Since fabrication of single crystal was difficult for bulk LLT samples, many researchers changed the strategy to synthesize single crystal LLT in thin film sample by epitaxial growth. Epitaxial growth, whose schematic processes shown in Figure 1.10, is very attractive to obtain single crystal thin film with particular orientation. It is a promising method for basic researches in physical properties and micro device applications. Materials in the upper layer tend to have the same crystal structure and the same crystal orientation as the single crystal substrate, enabling us to construct high quality single crystal thin films with well-defined crystallographic orientations. This characteristic advantage allows easier observation for physical properties. Besides, the epitaxial stress from substrate can strongly affect the thin film layer and stabilize the tensile and compressive epitaxial strain in the thin film under atmospheric condition.

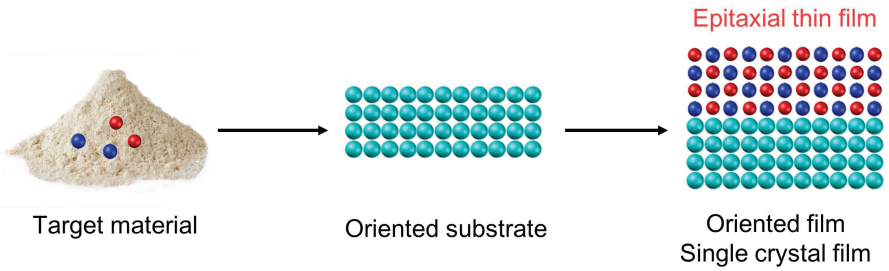

Figure 1.10 Schematic of epitaxial thin film growth.

Obtaining epitaxial LLT was still not easy and early thin film studies were almost based on polycrystalline, amorphous or composite samples. K. Kitaoka et al. first fabricated $Li_{0.5}La_{0.5}TiO_3$ thin films by sol-gel method on non-alkali aluminoborosilicate glass substrates with/without indium tin oxide coating [47]. Their LLT films were in

polycrystalline form with a preferred orientation of LLT(111) direction. O. Maqueda et al. deposited $Li_{0.33}La_{0.56}TiO_3$ thin films on polycrystalline α-Al_2O_3 substrates by pulsed laser deposition (PLD) [48] and obtained polycrystalline LLT with nanocrystalline structure. Several amorphous LLT thin film studies were published in the past decade by PLD method [49, 50]. However, most of them suffered from low ionic conductivity in these polycrystalline or amorphous thin film.

Epitaxial thin film study was first reported by M. Morcrette et al [51] in 1998. They fabricated 001 oriented LLT thin film with LLT 110 impurities on MgO (001) substrate by PLD method. M. Morales et al. followed this work by using radio frequency magnetron sputtering method in 2002 and reported detailed information of LLT 001/110 epitaxial relationship on MgO (001) substrates [52]. However, both of them suffered from high Li-loss during fabrication of thin films, resulting in very low ionic conductivity.

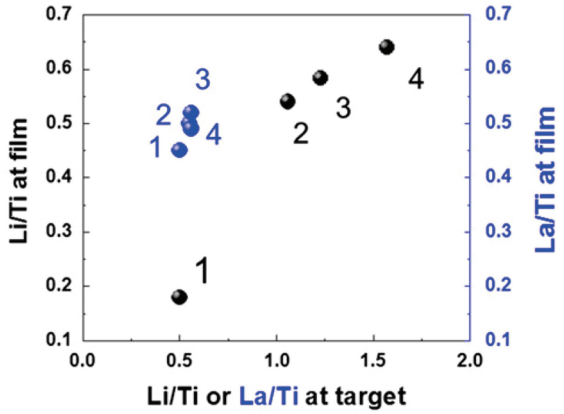

Figure 1.11 La/Ti and Li/Ti ratio in targets and films fabricated at 750 °C and oxygen pressure of 100 mTorr on Pt (111) substrates. Reprinted from Ref. [53], Copyright 2013, with permission from Elsevier.

D. H. Kim et al. first systematically studied the Li-loss of LLT thin film during PLD process [53]. By carefully analyzing Li/Ti ratio and La/Ti ratio in targets with various compositions and thin films fabricated from these targets, they claimed that more than 50% Li-loss was observed between the targets and thin films while the La/Ti ratio was

almost kept, as shown in Figure 1.11. Based on this result, they fabricated LLT epitaxial thin film on $SrTiO_3$ (100) substrate from a Li-rich $Li_{0.64}La_{0.49}TiO_3$ target and obtained LLT thin film with 001 orientation and some impurities.

In 2012, T. Ohnish et al. fabricated LLT epitaxial thin films on $SrTiO_3$ (100) and $NdGaO_3$ (110) from a stoichiometric $Li_{0.33}La_{0.56}TiO_3$ target by PLD method [54] and got phase pure LLT with 100 and 001 orientations, respectively. The in-plane ionic conductivity of the film grown on $NdGaO_3$ (110) substrate was 3.5×10^{-5} S/cm with an activation energy of 0.35 eV, while measurement on $SrTiO_3$ (100) failed for unknown reason. Although no boundary ionic conductivity was observed, such low ionic conductivity was possibly due to Li-loss. Similar to this research, K. Mitsuishi et al. fabricated $Li_{0.33}La_{0.56}TiO_3$ epitaxial thin film on Pt (111) substrate and analyzed the texture Nazca line structure [55], but their report lacks of information about composition and ionic conductivity.

R. Kanno's group fabricated $Li_{0.17}La_{0.61}TiO_3$ epitaxial thin films on Al_2O_3 (0001) and Nb:$SrTiO_3$ (111) substrates by PLD method and obtained phase pure LLT (111) thin films [56]. On Al_2O_3 (0001), they observed high in-plane ionic conductivity of 3.76×10^{-4} S/cm at room temperature, close to bulk ionic conductivity of polycrystalline bulk. They also fabricated a $SrRuO_3$(111) / $LiMn_2O_4$(111) / LLT(111) epitaxial heterostructure as a half electrode of battery on Nb:$SrTiO_3$ (111) substrate, showing reversible electrochemical reaction up to 4.5 V vs Li/Li^+ [57]. However, since LLT (111) direction is not the intrinsic Li diffusion path according to the bulk study, their films are not suitable for measuring the intrinsic property. In addition, out-of-plane ionic conductivity was not mentioned in this report.

In summary, epitaxial LLT thin film is a good solution to avoid low boundary ionic conductivity, though fabrication is still difficult mainly due to Li-loss. In addition, it

is also expected that tensile strain will lead to expansion of four-oxygen bottleneck for Li-hopping, considering from the results of bulk researches. More efforts to investigate its intrinsic properties are required in this research field including material synthesis and applications to battery.

1.5 Purpose of this study

As mentioned above, there are still many issues in the research field of LLT thin film growth, including Li-loss during film fabrication and low ionic conductivity. Also, effects of strain applied from substrates on ionic conductivity was not fully understood. Meanwhile, epitaxial thin films are suitable for studying strain controlled ionic conductivity which is not accessible in atmospheric condition in bulk samples. Moreover, the reason for failure in ionic conductivity measurements on $SrTiO_3$ substrates is unknown and no information was provided about the out-of-plane ionic conduction.

In this study, I focused on PLD fabrication of LLT epitaxial thin film along its intrinsic axis in perovskite structure. I investigated the effect of PLD parameters on Li-loss to fabricate stoichiometric phase pure LLT thin film with high quality. Different substrates with varied lattice constants were used to apply different strains on LLT thin film. I also studied the effect of in-plane epitaxial strain on ionic conductivity and crystal structure including lattice constant and orientations. LLT with conductive bottom electrode epitaxial heterostructure was fabricated to understand its out-of-plane ionic conductive behavior. In addition, interface between substrate, conductive electrode and LLT was characterized by X-ray reflection in order to investigate the multi-layer structures and the reason for failure of ionic conductivity measurements on $SrTiO_3$ substrates.

2 Experimental methods

2.1 Sample preparation

2.1.1 Pulsed laser deposition [58, 59]

Pulsed laser deposition (PLD) is a well-established technique for high-quality thin film fabrication. PLD is a specified physical vapor deposition technique using a high power laser beam to produce material source so that it allows deposition of materials with low vapor pressure. Since its invention in 1965 and success in fabricating high-temperature superconductor $YBa_2Cu_3O_{7-\delta}$ epitaxial thin film in 1987, this technique has become a common method for inorganic material thin film research.

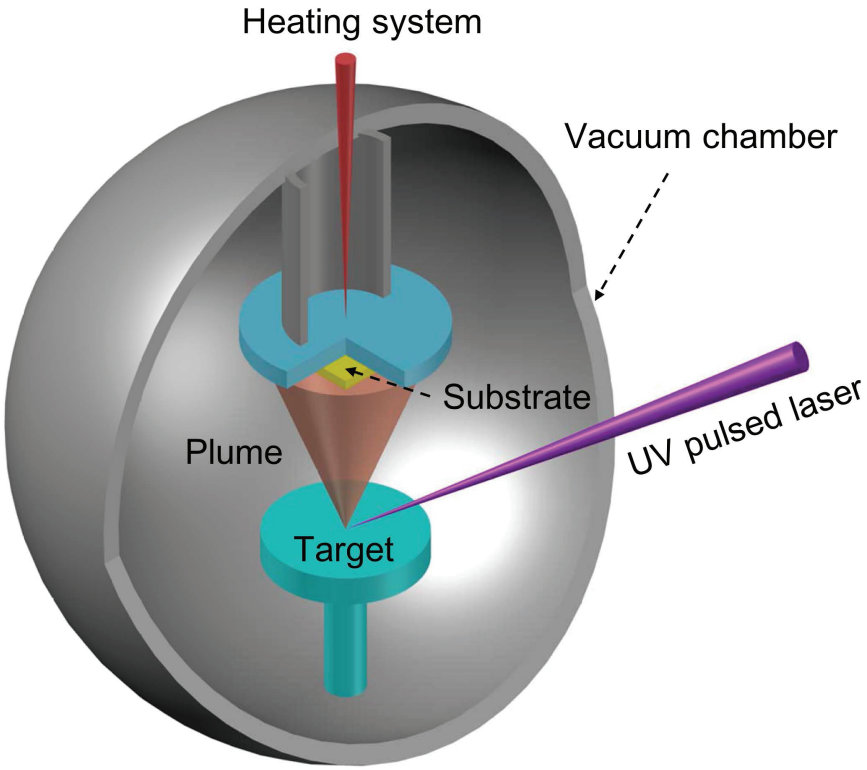

Figure 2.1 Schematic figure of PLD system

Figure 2.1 shows a schematic figure of typical PLD system. The system is composed of an ultrahigh vacuum chamber maintained by rotary pump and turbo molecular

pump, an ultraviolet pulsed laser, substrate heating system and focused optical systems. A target, which is used as a material source, is set at an angle of 45° to the laser beam. Parallel to the target surface, there is a single crystal substrate set above.

Pulsed laser deposition is considered to include the following processes [58, 59]:

- Light absorption in solid. When the target is irradiated with an ultraviolet pulsed laser, target surface absorbs the high energy of photons and is decomposed into particles and clusters containing ionized and atomic species. For a homogenous target, the energy absorption is similar for all the components in the target. If the intensity of laser beam within the laser spot is uniform, all components can evaporate in a stoichiometric way.

- Plasma generation. By a very complicated process during continuous photon excitation by the pulsed laser within ns-scale, species are injected perpendicular to the target surface to form a plasma and gain high kinetic energy with high density and temperature. As the excited temperature is extremely high, all the species are ionized with similar efficiency.

- Transfer of plasma. The generated plasma expands toward the substrate set right above under Coulomb repulsion and recoil, generating a spatial distribution of plasma called "plume". The plume size and spatial distribution of each species strongly rely on the scattering within the dense plasma and with molecules intentionally introduced in the chamber. The scattering yield is related with element mass, velocity of species, density of plume and background pressure [60, 61]. This will cause expansion of plume and give non-uniformity within the plume depending on the expanding angle.

- Deposition of film. When species in the plume reach the surface of substrate,

arriving atoms and ions will lose most of their kinetic energy and deposit as a thin film. Crystallization will also happen if enough energy for nucleation and surface migration is supplied by heating and interaction with substrate lattice. However, some of the species with low cohesive energy to substrate surface will be easily removed again from substrates due to collision of high energy species within the plasma, as called "re-sputtering effect". This will also cause non-stoichiometric transportation from target to substrates.

In early researches by PLD method, species are considered to be stoichiometrically transferred from target to substrate, without significant derivation of composition. However, many recent studies proved that PLD process may cause noticeable composition change of Li [62, 63], including Li-loss in LLT thin film study [53]. Therefore, precise control of parameters in PLD system is required to achieve the desired composition in thin film, including laser fluence, repetition rate, substrate temperature, background pressure and species, target composition and substrate.

In this work, I developed a PLD system equipped with a 248 nm KrF excimer (Coherent CompexPro 50) laser for target ablation. Laser ablation fluence was varied by a half-wavelength attenuator plate with fixed laser output energy and beam size. High-purity oxygen gas was introduced through a variable leak valve to control the background pressure. LLT targets were synthesized by solid state reaction and sintered as ceramic pellets. Several kinds of perovskite oxide single crystals were chosen as substrates for LLT thin film growth. Substrates were fixed on an oxidized Inconel alloy plate by Inconel clamps. Backside of the oxidized Inconel plate was irradiated by an 808 nm infrared laser. Substrate temperature was controlled by the output power of the infrared laser and monitored by a pyrometer.

2.2 Crystallography analysis

2.2.1 X-ray Diffraction [64, 65]

X-ray diffraction (XRD) is one of the most common and non-destructive method to obtain crystallography information of solid materials. X-ray has a wavelength at 10^{-10} m level, so that the diffraction can precisely reflect the crystal lattice structure with the same order. Since the penetration depth of X-ray is usually larger than film thickness, not only thin film lattice, but also the epitaxial relationship between thin film and substrate can be characterized by thin film XRD technique.

Principle of XRD can be described by reciprocal lattice and Laue's equation. Reciprocal lattice is the lattice of a crystal in its momentum space, or called *k*-space, whose spatial wavefunction is the Fourier transform of that in the original lattice. For a 3D lattice with infinite periods, the reciprocal lattice can be described as

$$\begin{aligned} \boldsymbol{b_1} &= 2\pi \frac{\boldsymbol{a_2} \times \boldsymbol{a_3}}{\boldsymbol{a_1} \cdot (\boldsymbol{a_2} \times \boldsymbol{a_3})} \\ \boldsymbol{b_2} &= 2\pi \frac{\boldsymbol{a_3} \times \boldsymbol{a_1}}{\boldsymbol{a_1} \cdot (\boldsymbol{a_2} \times \boldsymbol{a_3})} \\ \boldsymbol{b_3} &= 2\pi \frac{\boldsymbol{a_1} \times \boldsymbol{a_2}}{\boldsymbol{a_1} \cdot (\boldsymbol{a_2} \times \boldsymbol{a_3})} \end{aligned} \tag{2.1}$$

where $\boldsymbol{a_i}$ is the primitive vectors in the original lattice, $\boldsymbol{b_i}$ is the primitive vectors in the reciprocal lattice. The linear combination of these vectors forms reciprocal vector **G**,

$$\mathbf{G} = h\boldsymbol{b_1} + k\boldsymbol{b_2} + l\boldsymbol{b_3} \tag{2.2}$$

where *h*, *k* and *l* are respective integers representing indices of a reflection plane.

When X-ray is scattered by a lattice plane, the wavevectors of photons and lattice

vectors meet the Laue's equations:

$$\begin{aligned} \boldsymbol{a_1} \cdot (\boldsymbol{k_s} - \boldsymbol{k_i}) &= 2\pi h \\ \boldsymbol{a_2} \cdot (\boldsymbol{k_s} - \boldsymbol{k_i}) &= 2\pi k \\ \boldsymbol{a_3} \cdot (\boldsymbol{k_s} - \boldsymbol{k_i}) &= 2\pi l \end{aligned} \tag{2.3}$$

where $\boldsymbol{k_i}$ and $\boldsymbol{k_s}$ are the incident and scattered wavevectors, with a norm of $2\pi/\lambda$, respectively.

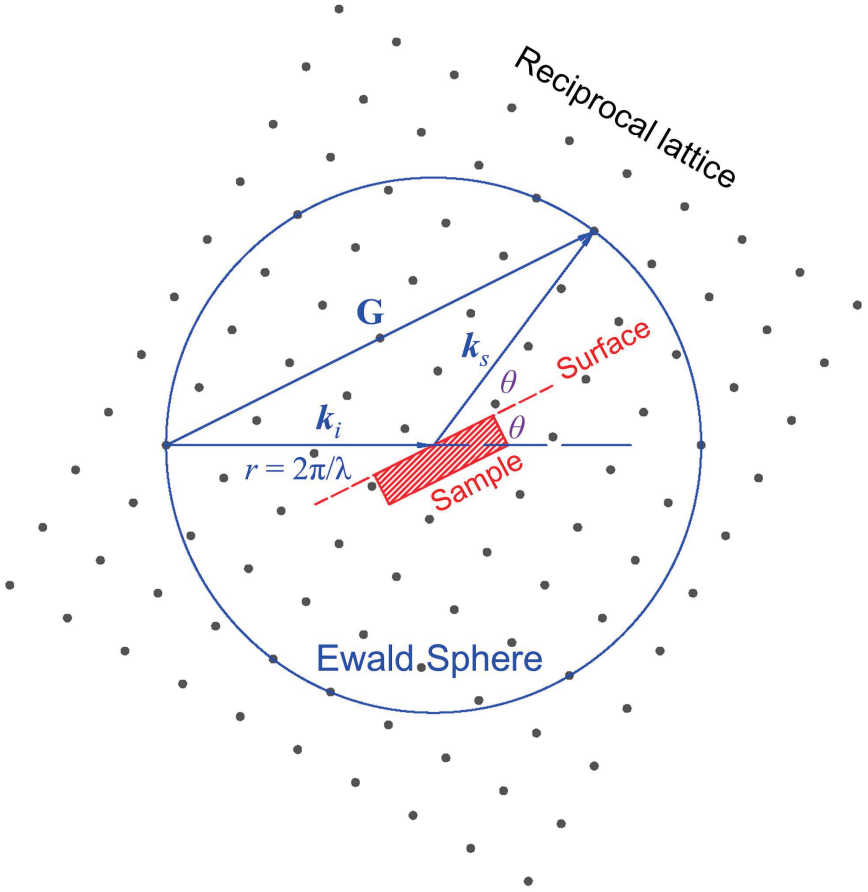

Figure 2.2 Cross section of Ewald sphere in a reciprocal lattice of cubic structure

One can find that only when $\mathbf{G} = \boldsymbol{k_s} - \boldsymbol{k_i}$, Laue's equations satisfy. Since XRD equipment has a fixed $\boldsymbol{k_i}$, the information of reciprocal vector $\mathbf{G}$ is obtained by measurement of scattered X-ray wavevector $\boldsymbol{k_s}$. In a perceptual intuition, one can draw a sphere with a radius of $2\pi/\lambda$ from the center of incident point and an axis representing incident

beam in the reciprocal space, called Ewald sphere (Figure 2.2). On the direction of $\boldsymbol{k_s}$ where diffraction is observed, there is a reciprocal lattice point at the intersection of $\boldsymbol{k_s}$ vector and Ewald sphere.

In a polycrystalline sample, crystals orient randomly, so that the diffractions on all the directions with the same cone vertex angle on Ewald sphere are equivalent, resulting in circular diffraction patterns. On the other hand, in a single crystal or oriented crystal such as epitaxial thin film, detailed information of crystal geometry results in a point-like diffraction pattern.

A typical 4-axis XRD equipment used for epitaxial thin film study is shown in Figure 2.3. Samples can be tilted along the azimuth direction described by an angle ω relative to the X-ray incident beam. Samples can also be tilted along the two altitude directions perpendicular to each other, described by angles χ and ϕ. The detector can move along another circular rail, in an angle 2θ to the X-ray incident beam. By controlling angles 2θ, ω, χ, ϕ, one can characterize crystal lattice by various mode, including

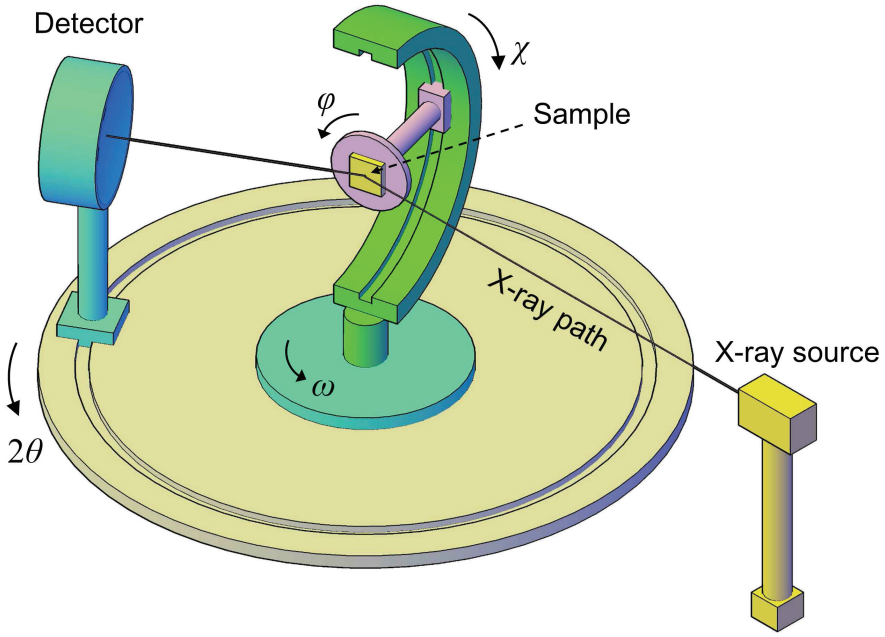

Figure 2.3 Schematic structure of 4-axis XRD equipment

- 2θ-θ scan: ω is fixed at half of 2θ. In this mode, Laue's equations can be converted to Bragg's law:

$$2d\sin\theta = n\lambda \tag{2.4}$$

where d is the distance between lattice planes perpendicular to the angle bisector of incident and scattered beams, λ is the wavelength of incident X-ray and n is an integer.

In epitaxial thin film analysis, one can specify the target lattice plane by tilting the angle χ and ϕ. Lattice constants can be calculated from Equation (2.4) through geometric relationships. The data are usually shown as 2θ-θ plots with 2θ as horizontal axis and diffraction intensity as vertical one. This is one of the most common scan modes in XRD measurement.

- Rocking curve: ω scan with fixed 2θ, χ and ϕ. The distribution of peak intensity can be obtained from this mode. Because real crystal does not have infinite lattice and is not perfect, and also X-ray generated from equipment is not perfectly coherent, XRD peaks will broaden and usually follow Gaussian distribution. The data are usually shown as rocking curves with ω versus diffraction intensity. The full width at half maximum (FWHM) of rocking curves is used as a measure of crystallinity, viz quality of crystals.

- Pole figure and ϕ-scan: ϕ scan with fixed 2θ, χ and ω. The symmetry of peaks can be determined by this mode. Since symmetry is determined by crystal structure, the same diffraction peak appears in equivalent directions. By rotating the sample along altitude ϕ direction, one can discover the number of equivalent directions and characterize the symmetry of crystal. In thin films, one can understand the epitaxial relationship between substrate and thin film through comparing the symmetry of each lattice. The data are usually shown as pole figure, which is the

stereographic projection of Ewald sphere from zenith pole, or ϕ-scan plots with ϕ versus diffraction intensity.

- Reciprocal space mapping (RSM): a cross section of reciprocal space. By performing 2θ-ω scan at each ω, cross section of reciprocal space is obtained. The data are usually converted to a map with $\boldsymbol{q}_x$ versus $\boldsymbol{q}_z$, where $\boldsymbol{q}_x$ and $\boldsymbol{q}_z$ are the inverse of lattice along in-plane and out-of-plane directions. Through RSM imaging, one can analyze the epitaxial relationship of crystal lattices between substrate and thin film.

In this study, XRD measurements were performed with a 4-axis diffractometer (Bruker AXS, D8 Discover). The equipment contains three kinds of detectors: 0D scintillation detector, 1D linear detector (VANTEC-1) and 2D detector (VANTEC-500) for different modes of measurements.

2.2.2 Reflection high-energy electron diffraction [66]

Reflection high-energy electron diffraction (RHEED) is also a technique using diffraction for characterization of lattice in solid materials. Different from XRD mentioned above, RHEED utilizes high energy electrons as an incident beam and it is very sensitive to surface lattice.

Figure 2.4 shows a typical setting of RHEED system. An electron gun ejects electrons with high energy of 10-50 keV. The electron beam irradiates on the sample surface at a very small angle and is reflected toward a monitor screen. Because of the grazing angle, the penetration depth of electron beams is 1 nm level so that only the information of surface lattice is obtained. RHEED system can be installed in a designed PLD vacuum chamber. Therefore in-situ monitoring of thin film growth is possible by RHEED measurement.

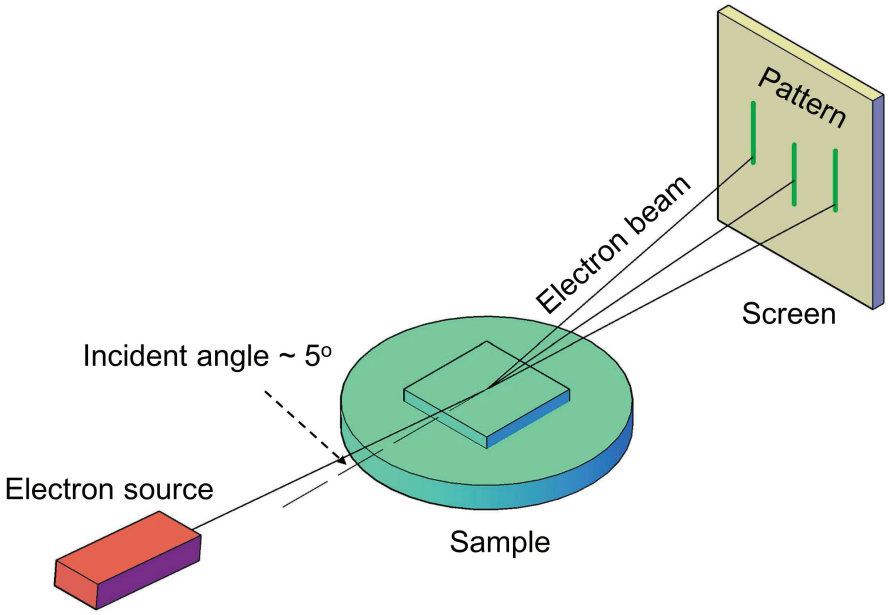

Figure 2.4 Schematic structure of RHEED

The principle of RHEED is similar to that of XRD. Since RHEED is surface sensitive, it is reasonable to apply 2D reciprocal lattice in this case. A 2D reciprocal lattice can be described as

$$\begin{aligned} \boldsymbol{b_1} &= 2\pi \frac{\boldsymbol{a_2} \times \boldsymbol{n}}{\boldsymbol{a_1} \cdot (\boldsymbol{a_2} \times \boldsymbol{n})} \\ \boldsymbol{b_2} &= 2\pi \frac{\boldsymbol{n} \times \boldsymbol{a_1}}{\boldsymbol{a_1} \cdot (\boldsymbol{a_2} \times \boldsymbol{n})} \end{aligned} \tag{2.5}$$

where $\boldsymbol{a_i}$ is the primitive vectors in the original lattice, $\boldsymbol{b_i}$ is the primitive vectors in the reciprocal lattice and $\boldsymbol{n}$ is the normal vector of lattice plane.

Since reciprocal lattice in 2D becomes rods perpendicular to the sample surface, typical RHEED image shows a rod like pattern for a flat surface. One can calculate the reflection angle 2θ from the geometry of equipment setting as well as the distance of rod patterns on the screen. Based on the obtained 2θ, the in-plane lattice constants can be calculated by using Bragg's law and lattice geometry. From the calculation result, information of in-plane lattice constant, in-plane symmetry, epitaxial relationship and surface reconstruction can be obtained.

Another important application of RHEED is in-situ observation of thin film growth process, especially layer-by-layer growth mode. In layer-by-layer growth, species will randomly distribute on the surface of thin film at first, and then form a perfect coverage before moving to the next layer. The intensity of RHEED during thin film growth will show a climax when one layer is formed and a minimal during random layer growth. This results in an oscillation in peak intensity and the period of oscillation represents the growth rate of thin film. In this study, RHEED system was installed on the PLD chamber for in-situ observation of thin film growth.

2.3 Structure analysis

2.3.1 Atomic force microscopy [67]

Atomic force microscopy (AFM) is a type of scanning probe microscopy with very high spatial resolution of the order of 1 nm. Using an AFM, it is possible to observe a sample surface at nanometer scale and analyze its roughness.

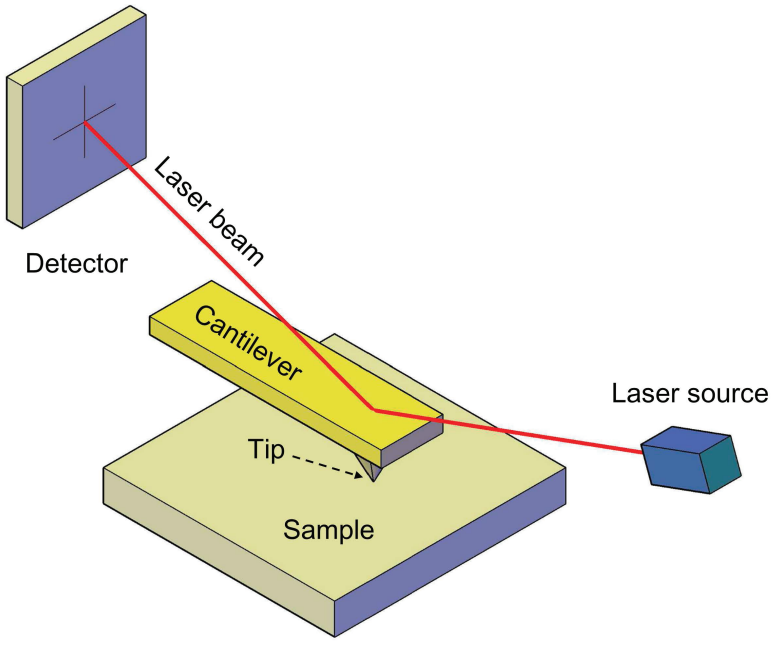

Figure 2.5 Schematic structure of AFM

Figure 2.5 shows a schematic of AFM system. The system contains a cantilever with tips whose apex consists of several atoms, a laser generator, an array-type photon detector and a sample stage controlled by piezoelectric driver. AFM measures the force between atoms, including van der Waals force, static electric force, Casimir effect and etc. If only van der Waals force is considered, the force can be considered in a very simple model described by Lennard-Jones potential as

$$V = A\left(\frac{1}{r}\right)^{12} - B\left(\frac{1}{r}\right)^{6} \tag{2.6}$$

where A and B are constants, r is the distance between a pair of neutral atoms.

Therefore, when the cantilever approaches the surface of sample, the atomic force changes with the distance between tip and surface atoms. This force induces bending of cantilever, resulting in a displacement of reflected beam by the back side of cantilever, which is measured by a photon detector. By probing sample surface through the displacement of reflected beam, the morphology of sample surface is observed. Because the tip apex is at atomic level, the spatial resolution can reach nanometer scale.

In this study, AFM measurements were performed by a commercial scanning probe microscopy system (SPI-4000, Hitach High Technologies).

2.3.2 X-ray Reflectometry [68]

X-ray reflectometry (XRR) is a technique to characterize the properties of thin films, including film thickness, surface roughness and density. It measures the intensity of reflected X-rays from a sample surface in relationship with incident angle.

XRR is a surface sensitive method. When the sample surface is perfectly flat, the reflection of X-rays will follow Fresnel conditions. The derivations from Fresnel condition can be measured to estimate the film properties mentioned above approximately as

given by L. G. Parratt:

$$R(Q) = R_{\mathrm{F}}(Q)\left|\frac{1}{\rho_\infty}\int_{-\infty}^{\infty} e^{iQz}\left(\frac{d\rho_e}{dz}\right)dz\right|^2 \tag{2.7}$$

where $R(Q)$ is the reflectivity, $R_{\mathrm{F}}(Q)$ is the Fresnel reflectivity representing a perfect reflection, Q is the momentum transfer of X-ray described as $Q = 4\pi\sin\theta/\lambda$, θ is the incident angle, λ is the wavelength of X-ray, z is the depth of sample, ρ_∞ is the density at infinite depth of the material and ρ_e is the average electron density profile in the sample.

Simulation of this equation yields the roughness of a sample surface and the density profile of a sample. For thin films grown on substrates and multilayers, XRR will show not only Fresnel reflectivity, but also oscillations. These oscillations can be explained by Fabry-Pérot effect: the X-rays reflected by the upper surface of thin film interference with the ones reflected by downer surface at characteristic incident angles related with thickness of thin films. Therefore, XRR is also used to analyze the thickness of thin film samples.

In this study, XRR was performed with the same instrument of XRD. Diffrac.Suite Leptos software package was used to simulate the depth profile of thin films measured by XRR.

2.4 Composition analysis

2.4.1 X-ray photoelectron spectroscopy [69]

X-ray photoelectron spectroscopy (XPS) is a technique to investigate electronic structures of materials and to measure elemental compositions quantitatively. According to photoelectric effect discovered by Einstein, electrons will escape from material surface by providing enough energy with photon irradiation. This technique detects the kinetic energy of electrons emitted by X-ray photon irradiation to examine the binding

energy of each electron using the following equation:

$$E_b = h\nu - E_k - \phi \tag{2.8}$$

where E_b is the binding energy of electron, $h\nu$ is the energy of X-ray photon, E_k is the kinetic energy of emitted electron measured by the instrument, ϕ is the work function related to machine and material.

As X-ray energy is high, not only valence electrons of elements, but also inner electrons can be emitted by X-ray beam, showing specific peaks of elements for qualitative analysis. In addition, the intensity of XPS peaks representing the number of electrons is related with the amount of corresponding element. By integrating the peak intensity in XPS spectra, quantitative analysis of chemical composition is also possible. However, for light elements such as Li, XPS has low efficiency to propagate photoelectrons due to the low binding energy. For these elements, only semi-quantitative analysis is possible.

In this study, XPS measurements were performed by a commercial XPS system (PHI5000 VersaProbe, ULVAC-PHI). Li compositions in LLT targets and thin films were semi-quantitatively analyzed by XPS.

2.4.2 Inductively coupled plasma optical emission spectroscopy [70]

Inductively coupled plasma optical emission spectroscopy (ICP-OES) is a quantitative analytical method to detect metal elements in solution at trace level. ICP-OES is based on two parts, excitation/ionization of sample in the inductively coupled plasma (ICP) and quantitative measurement by optical emission spectroscopy.

In ICP process, the solution samples are loaded with Ar gas into a fused silica tube as aerosols. The tube is surrounded with a coil. By controlling the frequency and power in the coil, strong and high frequency electromagnetic field is generated, resulting in the

formation of electron discharge at the outlet of silica tube. The generated electrons collide with Ar atoms and lead avalanche phenomenon of electron discharge, thus plasma is created with extreme high temperature up to 10000 K. Sample aerosol is converted into an atomic vapor within the plasma and gain enough energy for ionization and photon emission. Because the temperature of the plasma is sufficiently high, the ionization efficiency is usually more than 90% for metal species, enabling quantitative analysis for trace amounts.

After vaporization and ionization by ICP, the amount of each element are measured by optical emission spectroscopy. Because the elements are heated in the high-temperature plasma, electrons in atoms are excited from a lower energy level to a higher one by heat. The excited electrons are not stable so that they will lose their energy by emitting photons and transit to lower energy states. As the energy states of atoms are discrete, the light emission results in discontinuous spectrum and can be measured by a spectrometer. The discontinuous spectrum is characteristic for each element according to the electronic structure. By observation of the designated wavelength and its intensity, qualitative and quantitative information of each element is obtained.

In this study, ICP-OES measurements were performed by a commercial ICP-OES instrument with external standard method for La and Ti composition analysis. ICP-OES was not suitable for Li analysis because an emission line of Ar gas partially overlapped with that of Li.

2.4.3 Atomic absorption spectroscopy [71]

Atomic absorption spectroscopy (AAS) is a technique based on the light absorption of atoms. Absorption is just the opposite process of emission. In absorption spectroscopy, samples are evaporated to provide atoms in the most stable ground state. Because the

energy levels are discrete in atoms, the electrons in the ground state can absorb light with a characteristic wavelength and be excited to a higher energy level. The degree of light absorption increases as the number of atoms increases. Therefore the quantitative analysis is possible.

Ideally, the light absorption in a homogenous sample can be described by Beer-Lambert law as

$$A = \log_{10}\frac{I_t}{I_0} = \varepsilon \cdot l \cdot c \tag{2.9}$$

where A is the absorbance of sample, I_0 and I_t are the luminous intensity of incident and transmitted light, ε is the molar attenuation coefficient, l is the thickness of sample and c is the concentration of measured species.

According to Beer-Lambert law, concentration is proportional to absorbance. However, in most of the cases, the relationship between concentration and absorbance is not linear, because of various reasons including matrix effect of solution, low ionization efficiency, non-homogenous evaporation, absorption by nearby lines and etc. Therefore, calibration by standard solutions is necessary.

In this study, a graphite furnace atomic absorption spectroscopy (GFAAS) instrument was used for Li composition analysis. Samples were transferred on a piece of graphite and heated to atomic vapors. A hollow-cathode lamp with wavelength of 670.78 nm was used as a light source. Quantitative analysis was carried out by external standard method.

2.5 Ionic conductivity analysis

2.5.1 Electrode preparation

In order to measure in-plane ionic conductivity, microelectrodes were patterned by photolithography and deposited by electron beam evaporation in an ultrahigh vacuum chamber. Photolithography is a technique to fabricate designed micro patterns on thin films or surface of bulk substrates.

A typical schematic of electrode preparation is shown in Figure 2.6.

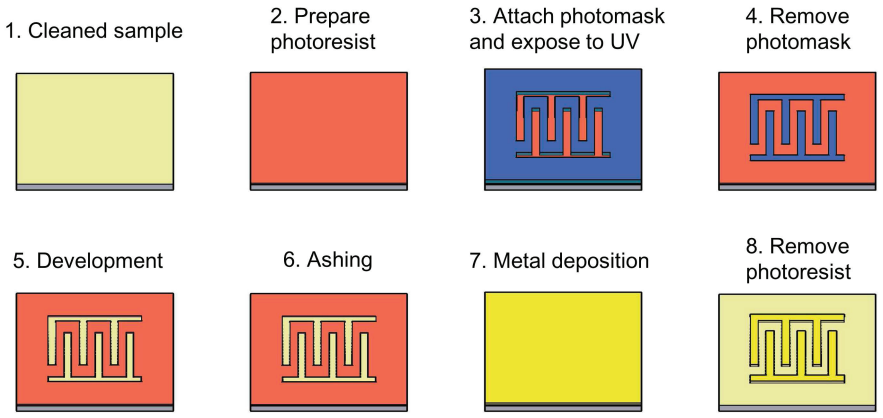

Figure 2.6 Schematic process of electrode preparation by photolithography

The detail processes are:

- Cleaning: The sample is cleaned to remove surface contaminations.
- Photoresist preparation: A layer of photosensitive polymer, which is called "photoresist", is coated on the sample and dried by heating.
- Exposure: The prepared photoresist is covered with a photomask, which is made of a piece of glass coated with Cr metal patterns. After alignment of the photomask to specified position, UV light is irradiated through the transparent parts of photomask and make the photoresist exposed.

- Developing: A part of photoresist is removed by a selected solvent, called "developer", and rinsed in another solution to remove the photoresist thoroughly. Generally, there are two kinds of photoresist, positive photoresist whose exposed parts are removed and negative photoresist whose non-exposed parts are removed.
- Ashing: Sample surface is cleaned with ozone plasma to remove contaminations from the developing process.
- Electrode deposition: The cleaned sample is transferred into an ultrahigh vacuum chamber. Electrodes are deposited by electron beam evaporation method.
- Remove photoresist: After the electrode deposition, the remained photoresist is removed by a specified solvent called "remover" as well as the metal covered above.

In this study, microelectrodes were prepared on thin film samples by using a positive photoresist and deposited with Ti/Au metals. All these processes were performed in a clean room to avoid dust contamination.

2.5.2 Electrochemical impedance spectroscopy [72]

Electrochemical impedance spectroscopy (EIS) is a technique to measure the current and voltage as well as the phase angle in relation with frequency of an alternating current (AC) circuit. EIS is usually used to analyze ionic conductivity, dielectric property, and electrode-electrolyte interface in electrochemical reactions.

The impedance, which is the opposition to a current when applying a voltage, is defined as the complex ratio of the voltages to the currents, with a symbol Z in usual. The data of impedance spectroscopy are usually plotted as Cole-Cole plots (or Nyquist plots) with the real part of impedance versus the imaginary one, and Bode plots with two curves composed of the impedance versus frequency curve and the phase angle versus

frequency curve.

In a circuit where electrons take the role of charge transfer, the impedance values of resistor, capacitor, inductor, series connection and parallel connection are described as Table 2.1, where ω is the angular frequency given by $\omega = 2\pi f$, f is the frequency of AC circuit, R is the resistance, C is the capacitance, L is the inductance and Z_i is the component of series or parallel circuits. These device elements are very important in analysis of electronic devices, especially dielectric constants of materials.

Table 2.1 Impedance values of elements in a circuit

Element	Current vs Voltage	Impedance
Resistor	$V = IR$	$Z = R$
Capacitor	$C\frac{dV}{dt} = I$	$Z = \frac{1}{i\omega C}$
Inductor	$V = L\frac{dI}{dt}$	$Z = i\omega L$
Series		$Z = \sum_1^n Z_i$
Parallel		$\frac{1}{Z} = \sum_1^n \frac{1}{Z_i}$

On the other hand, in electrochemical reactions and ionic conductive materials, the charge transfer is conducted by ions, which also cause mass transfer. The diffusion of mass becomes important in this case and diffusion elements have to be considered in the impedance spectrum. The diffusion of mass can be considered as linear diffusion following Fick's law. For a semi-infinite linear diffusion, it can be described as

$$\frac{\partial c}{\partial t} = D\frac{\partial^2 c}{\partial x^2} \tag{2.10}$$

where c is the concentration of ions, x is the coordination for diffusion and D is the diffusion coefficient. Taking a Laplace transform to Equation (2.10), one can get the solution for c

$$s \cdot c - c|_{t=0} = D\frac{d^2c}{dx^2} \tag{2.11}$$

$$s = \sigma + i\omega \tag{2.12}$$

$$\Delta c = c|_{t=t} - c|_{t=0} = Ae^{-\alpha x} + Be^{\alpha x} \tag{2.13}$$

$$\alpha = \sqrt{s/D} \tag{2.14}$$

where σ and ω are real constants, A and B are constants, s is the complex frequency, Δc is the excess of concentration.

By applying Nernst equation as Equation (2.15) and considering the charge transfer relationship as Equation (2.16), the voltage and current are

$$\Delta V = \frac{k_B T}{ne}\ln\frac{c+\Delta c}{c} \approx \frac{k_B T}{ne}\frac{\Delta c}{c} \tag{2.15}$$

$$\Delta I = neJ = -neAD\frac{dc}{dx} = -neAD(\Delta c)' \tag{2.16}$$

where k_B is the Boltzmann constant, T is the temperature, J is the current density, n is the number of transferred charge, e is the charge of electron and A is the cross-section area of diffusion.

If sinusoidal voltage with angular frequency ω is applied, $\sigma = 0$. When the system meets semi-infinite boundary condition $\Delta c \to 0$ as $x \to \infty$, the solution of Δc and impedance Z at the interface are

$$\Delta c = \Delta c_0 e^{-\sqrt{i\omega/D}x} \tag{2.17}$$

$$Z_W = \left(\frac{\Delta V}{\Delta I}\right)_{x=0} = \frac{k_B T}{n^2 e^2 ADc}\frac{1}{\sqrt{i\omega/D}} \tag{2.18}$$

This element Z_W is called infinite Warburg element describing diffusion in electrochemical reaction and ionic conductive behavior. In Cole-Cole plots, infinite Warburg elements show an infinite ray with a phase angle of 45°.

In actual measurements, blocking electrodes are usually used where ions cannot intercalate. Finite-length Warburg element has to be calculated. Suppose the diffusion length is δ. The boundary condition at $x = \delta$ can be considered as zero flux Neumann boundary condition $(\Delta c)' = 0$. Therefore the boundary condition, concentration c and impedance Z can be described as

$$\Delta c = B\cosh\left[\sqrt{\frac{i\omega}{D}}(\delta - x)\right] \tag{2.19}$$

$$Z_{W\,fin} = \left(\frac{\Delta V}{\Delta I}\right)_{x=0} = \frac{k_B T}{n^2 e^2 A D c}\frac{\coth(\sqrt{i\omega/D}\delta)}{\sqrt{i\omega/D}} \tag{2.20}$$

This element $Z_{W\,fin}$ describes the diffusion with finite-length and blocking electrode at boundary, showing a line with a finite length and phase angle of 45° in high frequency part and a capacitor-like signal in low frequency part of Cole-Cole plots.

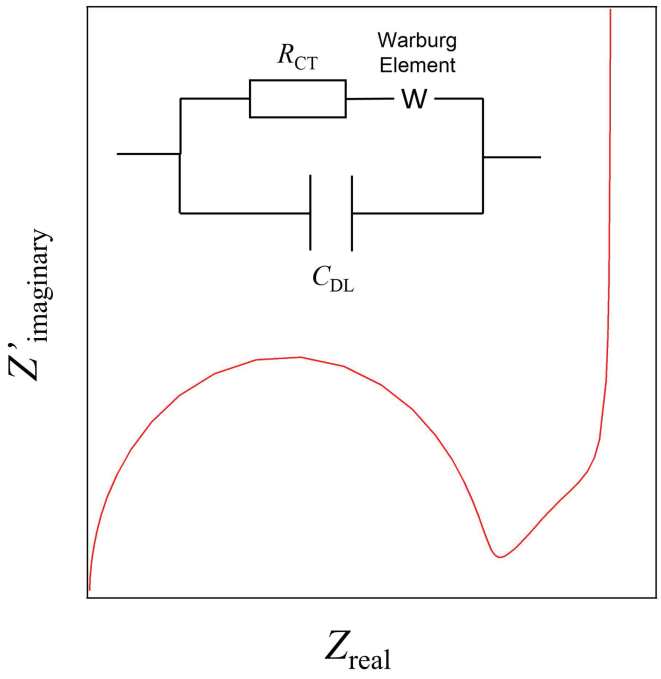

Figure 2.7 Cole-Cole plot for a Randle circuit shown in the inset

For ionic conductivity measurement using blocking electrode, a Randle circuit is used to simulate the data. Figure 2.7 shows a Randle circuit and the corresponding Cole-Cole plot. In the Randle circuit, the resistor represents the charge transfer resistance of

ion migration. The capacitor element represents the double layer capacitance between electrode and electrolyte. Knowing the resistance of charge transfer, one can calculate the ionic conductivity from the simulated resistance, while simulated capacitance indicates the specified type of ionic conductive behavior in the materials.

In this study, impedance spectroscopy was conducted by an impedance analyzer (Solartron 1260+1296) and a prober system for microelectrodes with hot plates under atmosphere.

3 Thin film growth of $Li_{0.33}La_{0.56}TiO_3$ and strain-controlled ionic conductivity*

3.1 Introduction

As introduced in Chapter 1, lithium lanthanum titanates $Li_{3x}La_{2/3-x}TiO_3$ (LLT, $0.05 < x < 0.167$) are very promising materials for solid state lithium ion electrolytes. Among all of them, $Li_{0.33}La_{0.56}TiO_3$ has the highest bulk ionic conductivity up to 1.3 mS/cm. In order to solve the problem of low ionic conductivity at boundaries in polycrystalline samples, I describe the epitaxial thin film growth of LLT on $SrTiO_3$ (100), $(LaAlO_3)_{0.3}$-$(SrAl_{0.5}Ta_{0.5}O_3)_{0.7}$ (100) and $NdGaO_3$ (110) substrates by pulsed laser deposition method (PLD) in this chapter. The dependence of Li-composition in thin film on laser fluence during PLD process was investigated. An optimized fabrication condition was discovered and the influence of epitaxial strain on lattice parameters and orientations was discussed. The ionic conductivity of LLT on $NdGaO_3$ (110) substrate was successfully measured and its strain-controlled ionic conductive behavior was studied.

3.2 Experimental methods

Stoichiometric $Li_{0.33}La_{0.56}TiO_3$ and Li-rich $Li_{0.84}La_{0.56}TiO_{3+\delta}$ were synthesized by solid state reaction for PLD target. Li_2CO_3, TiO_2 and as-dried La_2O_3 powders (Wako Pure Chemical) were mixed with prescribed amounts and sintered at 850 °C for 12 h in air. The sintered powders were milled and pressed into pellets under 40 MPa. The pellets were sintered again at 1200 °C for 12 h in air.

*A part of this chapter (including Figures 3.1 to 3.3, 3.6 to 3.9, 3.16 and 3.18) has been published in *Crystal Growth & Design.* Reprint with permissions from "Epitaxial Strain-Controlled Ionic Conductivity in Li-Ion Solid Electrolyte $Li_{0.33}La_{0.56}TiO_3$ Thin Films", Jie Wei, Daisuke Ogawa, Tomoteru Fukumura, Yasushi Hirose and Tetsuya Hasegawa, *Cryst. Growth Des.,* **2015,** *15*(5), 2187-2191. Copyright 2015 American Chemical Society.

LLT thin films were deposited on $SrTiO_3$ (100) (STO, cubic a = 0.3905 nm), $(LaAlO_3)_{0.3}$-$(SrAl_{0.5}Ta_{0.5}O_3)_{0.7}$ (100) (LSAT, cubic a = 0.3868 nm) and $NdGaO_3$ (110) (NGO, orthorhombic a = 0.5431 nm, b = 0.5499 nm, c = 0.7710 nm) single crystal substrates by PLD method. STO (100) substrates with step and terrace surface were obtained from BHF pre-treated as-purchased ones by annealing at 1050 °C for 2 h in air. LSAT (100) and NGO (110) substrates were annealed in air for 2 h at 1000 °C for flatter surface. KrF excimer laser (Coherent COMPexPro 50) with wavelength of 248 nm was used for deposition. The laser fluence was varied by a half-wave attenuator module from 0.5 to 2 J/cm^2 at an ablation frequency of 10 Hz. In addition, substrate temperature and oxygen partial pressure were varied for thin film crystallinity optimization.

Crystal structures of LLT thin films were analyzed by XRD (D8 Discover, Bruker). Surface morphology was measured by AFM (SPI-4000, Hitachi High Technologies). Thickness was evaluated by a stylus profilometer (Dektak XT, Bruker). Thin film compositions were analyzed by XPS (PHI 5000 Versaprobe, ULVAC-PHI), ICP-OES and GFAAS. The ionic conductivity was studied by impedance spectrum (Solatron 1260+1296) with a prober system in air.

3.3 Results and discussions

3.3.1 Laser fluence dependence of Li-composition

LLT thin films fabricated from stoichiometric $Li_{0.33}La_{0.56}TiO_3$ targets had been studied primarily in my master dissertation [73]. However, the Li-compositions in thin films were much lower than those in targets. In order to understand what affects the Li-composition, I first performed the PLD growth in vacuum (10^{-8} Torr) at room temperature. As a result, I was able to focus on how laser fluence affects the Li-composition without the influence of evaporation at high growth temperature and scattering by back-

ground high pressure oxygen.

Figure 3.1 shows the Li 1s peak of amorphous LLT thin films fabricated from a stoichiometric $Li_{0.33}La_{0.56}TiO_3$ target at different laser fluences, normalized to Ti 2p peaks for comparison. Powder $Li_{0.33}La_{0.56}TiO_3$ sample was used as a reference (black line). In this figure, it is clear that the Li 1s peak intensity dropped when laser fluence increased. As evaporation due to substrate heating and scattering by background oxygen were not considerable, this result indicates that Li composition strongly depended on laser fluence.

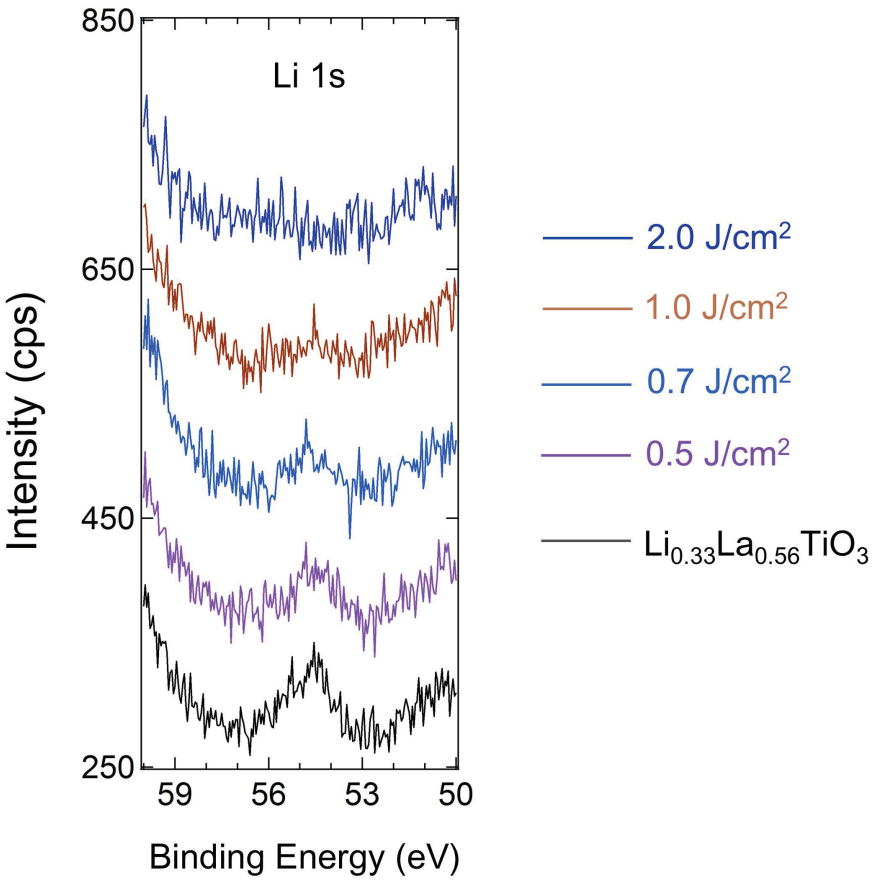

Figure 3.1 XPS for Li 1s peaks of amorphous LLT thin films on STO (100) substrates. Powder $Li_{0.33}La_{0.56}TiO_3$ was used as a reference (black line). The spectra are shifted vertically for convenience.

The dependence of Li composition in thin film on laser fluence can be explained by two causes: plume expansion and re-sputtering.

Plume expansion

Plume expansion can be explained by the model of K. L. Saenger [61]. In the model, deposition profile D is defined as the unit probability for particles leaving the source to deposit on the substrate, as Equation (3.1).

$$D(\theta,\phi) \equiv D(\Omega) = \frac{d\Omega}{dA}\int_0^\infty f(v,\Omega)dv \tag{3.1}$$

where Ω is the solid angle of the particles, v is the speed of the particles, $f(v,\Omega)$ is the probability density function of the particles following Maxwell-Boltzmann distribution, dA is the area on the substrate, and θ and ϕ are the polar and azimuth angle measured from a fixed zenith direction perpendicular to the target surface, respectively. After some arrangement, the equation becomes

$$D(\theta) \approx \frac{B'}{h^2}\cos^4\theta e^{-(\gamma/2)\widetilde{M}\sin^2\theta} \times \sum_{l=0}^{3} a_l \left[\left(\frac{\gamma}{2}\right)^{1/2}\widetilde{M}\cos\theta\right]^l \tag{3.2}$$

$$\widetilde{M} = u/(\gamma kT/m)^{1/2} \tag{3.3}$$

where B' is a constant, $\widetilde{M}$ is the Mach number, $\gamma = C_p/C_v$ is the specific heats ratio of constant pressure and volume, u is the flow velocity, T is the temperature, and a_l are constants. From this model, species with higher $\widetilde{M}$ have smaller $D(\theta)$ at higher θ and larger $D(\theta)$ at lower θ, so that they are more concentrated on the on-axis substrate direction where θ is rather small. Therefore, species with higher $\widetilde{M}$ will have relatively higher compositions in thin film.

For a gas mixture with multiple species, Mach number of each species is given by

$$\widetilde{M}_{F_j} = \sqrt{\frac{2}{\gamma-1}\frac{m_j}{m_{\text{avg}}} \times \frac{T_0}{T_{F_j}}\left(1-\frac{T_{F_j}}{T_0}\right)} \tag{3.4}$$

where $\widetilde{M}_{F_j}$ is the Mach number of species j, m_j is the mass of species j, m_{avg} is the average mass of all species, T_0 is the original temperature of plume after ablation, T_{F_j} is the freezing temperature defined as the temperature when species commence free molecular flow after cooling of adiabatic expansion.

Under a high laser fluence of LLT growth, laser plume showed strong expansion, where all the species tended to have the same T_{F_j}. According to Equation (3.4), heavier elements Ti and La with larger mass m_j appeared with larger Mach number $\widetilde{M}_{F_j}$. Thus they tended to concentrate on the on-axis substrate direction according to Equation (3.2). On the other hand, light element Li has smaller $\widetilde{M}_{F_j}$ due to its smaller m_j. In this case, Li showed relatively lower composition on the on-axis direction. In summary, a high laser fluence reduced the Li composition on the substrates due to the strong expansion.

Under a low laser fluence of LLT growth, laser plume showed weak expansion and each species tended to have different T_{F_j}. Since the heavier elements La and Ti tended to have relatively lower speed due to the higher mass, their collision rates were smaller and appeared with smaller change of velocity after collision. This results in a faster cooling rate during adiabatic expansion, so that the heavier elements La and Ti showed higher T_{F_j} and lower Mach number $\widetilde{M}_{F_j}$. On the other hand, the lighter element Li tended to collide more frequently and to maintain its speed after collision during adiabatic expansion. It showed a lower freezing temperature T_{F_j}, resulting in relatively higher Mach number $\widetilde{M}_{F_j}$. Therefore, under a low laser fluence, Li composition in thin film growth on on-axis direction was relatively higher than that under a high laser fluence.

Re-sputtering effect

With an increasing laser fluence, the kinetic energy of particles in the plume also increases. The grown thin film can be sputtered by the ablated particles, leading to low growth rates. The sputtering yield Y for a single component self-sputtering, defined as the ratio of removed atoms and incident atoms, is given by P. C. Zalm [74] as

$$Y \simeq \frac{5}{3} C_{pt} \left(\frac{\sqrt{E} - \sqrt{8U_0}}{\sqrt{E_{pt}}} \right) \tag{3.5}$$

where E is the kinetic energy of incident particles, U_0 is the cohesive energy to prevent the surface escaping of sputtered species, C_{pt} and E_{pt} are the characteristic parameters related to projectile and target species. This equation indicates that sputtering becomes more significant when the kinetic energy E of incident particles is higher. Therefore, a high laser fluence causes strong re-sputtering effect of thin films in PLD process.

For multi-component thin films, J. Schou [60] gave a ratio of sputtering yield between two components as

$$\frac{Y_A}{Y_B} = \left(\frac{m_B}{m_A}\right)^{2m} \left(\frac{U_B}{U_A}\right)^{1-2m} \left(\frac{c_A}{c_B}\right) \tag{3.6}$$

where m_A and m_B are the masses of element A and B with concentrations of c_A and c_B and cohesive energy of U_A and U_B, respectively, and $m \approx 0.1$ is a constant calculated from Coulomb interaction potential. From Equation (3.6), the element with the lowest cohesive energy and the lightest mass is influenced by the strongest re-sputtering effect. In LLT thin film, Li (U_{Li} = 158 kJ/mol) has lower cohesive energy and mass than La (U_{La} = 431 kJ/mol) and Ti (U_{Ti} = 468 kJ/mol) [75]. Therefore, Li suffered the strongest re-sputtering effect among all elements.

To summarize this part, I found that the Li composition in amorphous LLT thin film depends on laser fluence. This can be explained by two causes, the plume expansion effect and the re-sputtering effect. Under an increased laser fluence, the lightest element Li tended to have a wider spatial distribution, resulting in Li-loss in the center on-axis substrate position. Also, the lowest cohesive energy of Li to solid surface engendered the strongest re-sputtering effect at a high laser fluence. From this phenomenon, I believed that a low laser fluence was important to obtain stoichiometric $Li_{0.33}La_{0.56}TiO_3$ thin films.

3.3.2 Laser fluence dependence of thin film growth rate

The thin film growth rate of epitaxial LLT was studied. Following the preliminary work on the crystallization temperature and oxygen pressure during PLD growth in my master course [73], LLT thin films were fabricated at 950 °C in oxygen pressure of 50 mTorr from a $Li_{0.33}La_{0.56}TiO_3$ target to investigate the growth rate. The laser fluence was adjusted as 0.7, 1.0, 1.2, 1.4 J/cm^2.

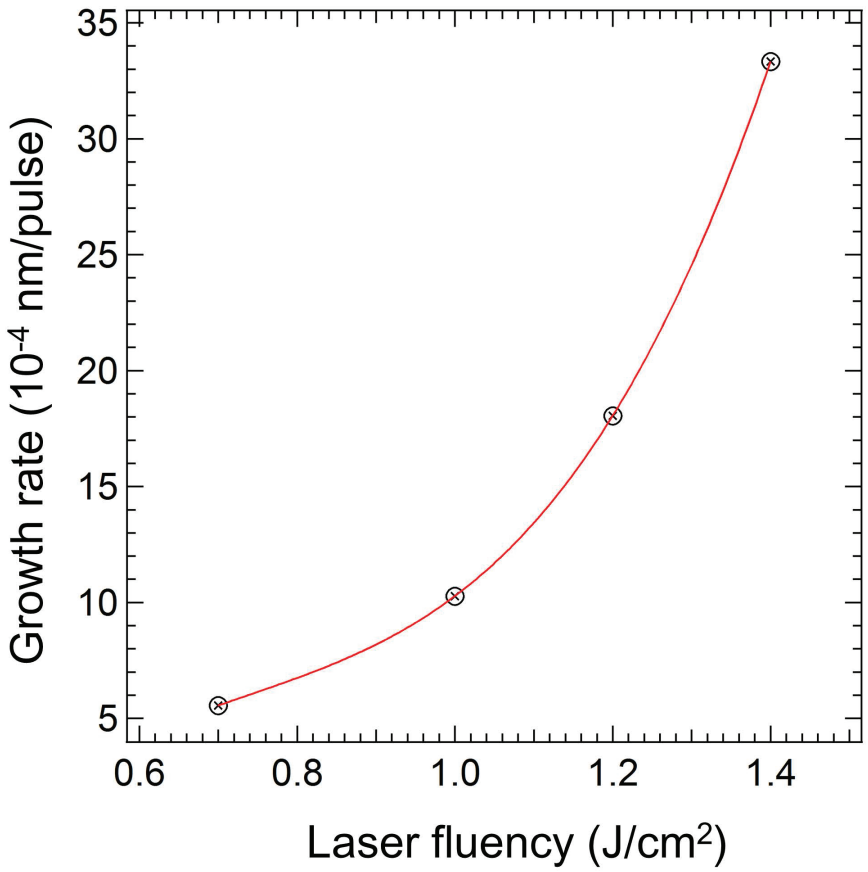

Figure 3.2 Laser fluence dependence of growth rate for LLT epitaxial thin film fabricated from a stoichiometric $Li_{0.33}La_{0.56}TiO_3$ target at 950 °C in oxygen pressure of 50 mTorr.

Figure 3.2 shows the growth rate of epitaxial LLT thin film at different laser fluences. The growth rate dropped significantly when laser fluence decreased. As discussed above, a low laser fluence is preferred to avoid Li-loss in PLD process. However, at a low laser fluence, it took very long time (5 - 6 h) to obtain thin film with $>$ 50 nm thick-

ness for further study. This generated another difficulty to obtain homogenous thin film due to the long time deposition.

In order to compensate the Li-loss during PLD process and fabricate homogenous LLT thin films at an acceptable deposition rate, a Li-rich target was used for the following LLT thin film growth.

3.3.3 Optimization of LLT thin film growth

Laser fluence

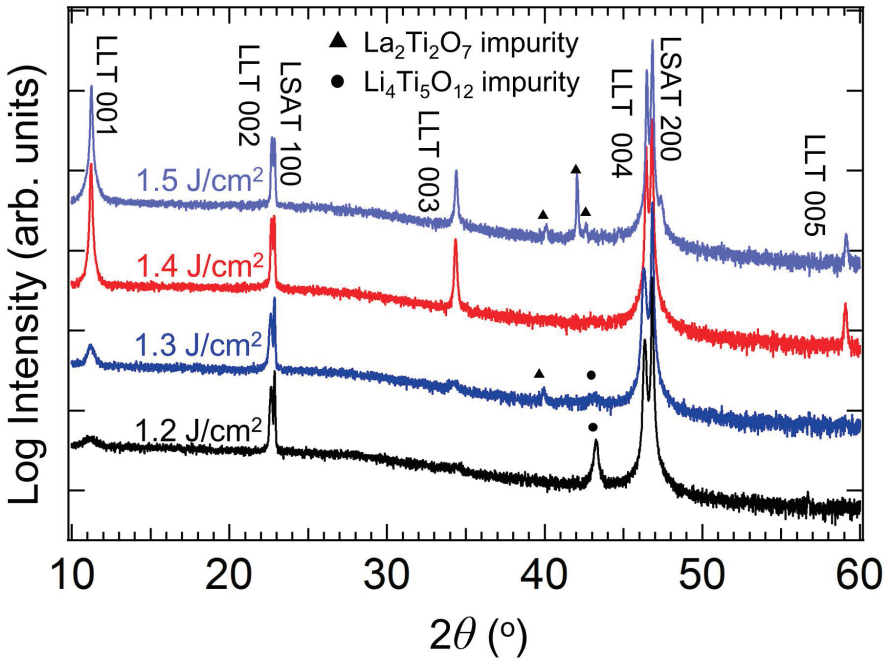

Figure 3.3 Out-of-plane 2θ-θ XRD patterns for LLT thin films on LSAT (100) substrates, grown at substrate temperature of 950 °C in oxygen pressure of 50 mTorr with different laser fluences.

LLT thin films were fabricated on LSAT (100) substrates from a Li-rich $Li_{0.84}La_{0.56}TiO_{3+\delta}$ target at 950 °C in oxygen pressure of 50 mTorr. The laser fluence was adjusted from 1.2 to 1.5 J/cm^2. Figure 3.3 shows the out-of-plane 2θ-θ XRD patterns for LLT thin films. With a low laser fluence of 1.2 and 1.3 J/cm^2, LLT 004 appeared with small LLT 001 peaks, together with Li-rich impurity $Li_4Ti_5O_{12}$ phase. With a high laser flu-

ence of 1.5 J/cm^2, pyrochlore $La_2Ti_2O_7$ phase was observed. Only at an intermediate laser fluence of 1.4 J/cm^2, pure LLT phase was observed. This result indicates that Li composition in epitaxial LLT thin films increases by decreasing the laser fluence, which is consistent with the result discussed above in amorphous LLT thin films.

Temperature

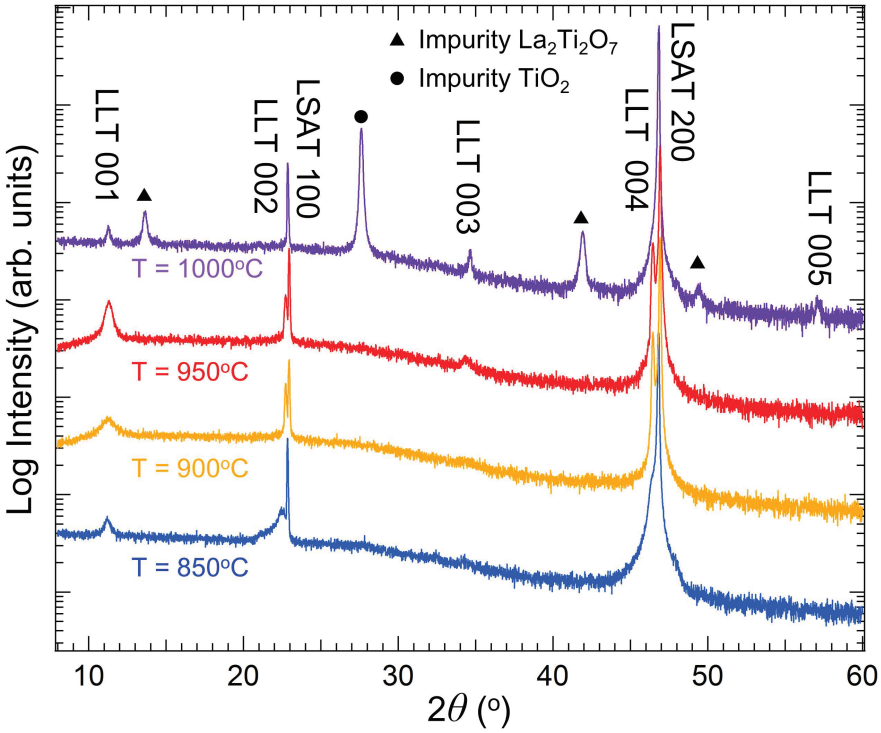

Figure 3.4 Out-of-plane 2θ-θ XRD patterns for LLT thin films on LSAT (100) substrates, grown in oxygen pressure of 50 mTorr with a laser fluence of 1.4 J/cm^2 under different substrate temperatures.

LLT thin films were fabricated on LSAT (100) substrates from a Li-rich $Li_{0.84}La_{0.56}TiO_{3+\delta}$ target in oxygen pressure of 50 mTorr with a laser fluence of 1.4 J/cm^2. The fabrication temperature was varied from 850 °C to 1000 °C. Figure 3.4 shows the out-of-plane 2θ-θ XRD patterns of LLT thin film at each temperature. It is clear that at a high temperature of 1000 °C, LLT partially decomposed as seen from the appearance of TiO_2 and $La_2Ti_2O_7$ impurities with weakened LLT peaks, due to the high volatility of

Li. At a low temperature of 850 °C and 900 °C, crystallization of LLT thin films were not at its optimal. Therefore, a substrate temperature of 950 °C was considered as the best condition.

Oxygen pressure

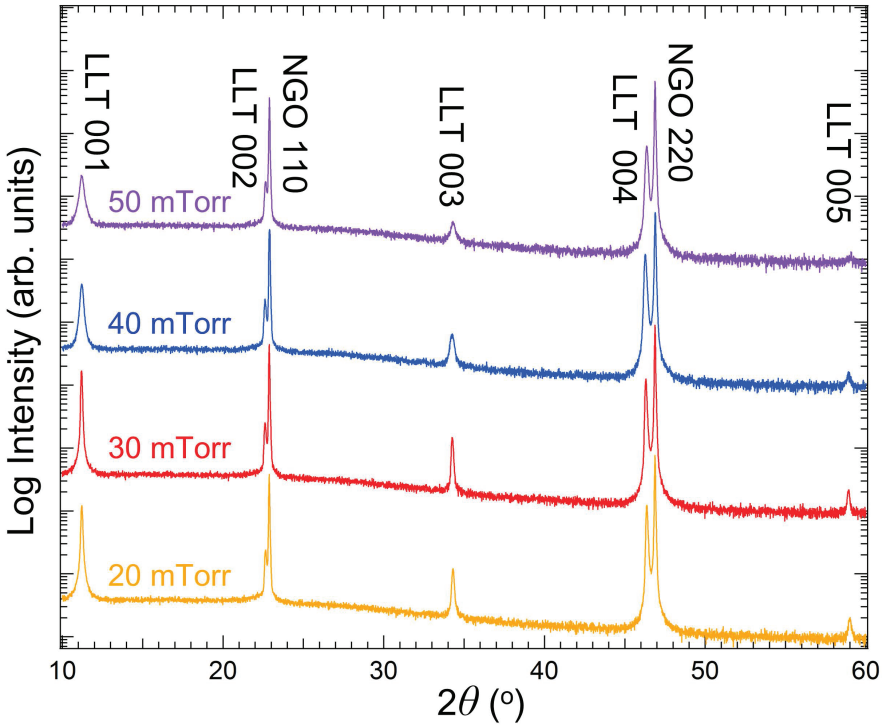

Figure 3.5 Out-of-plane 2θ-θ XRD patterns for LLT thin films on NGO (110) substrates, grown at substrate temperature of 950 °C with a laser fluence of 1.4 J/cm^2 under different oxygen pressure.

According to my previous work in master dissertation [73], LLT thin films required an oxygen pressure higher than 10 mTorr, otherwise anatase TiO_2 impurity appeared. Here, LLT thin films were fabricated on NGO (110) substrates from a Li-rich $Li_{0.84}La_{0.56}TiO_{3+\delta}$ target at 950 °C with a laser fluence of 1.4 J/cm^2. The oxygen pressure was adjusted from 20 mTorr to 50 mTorr. Figure 3.5 shows the out-of-plane 2θ-θ XRD patterns of LLT thin film at various oxygen pressures. LLT 001 and 003 peaks reached a climax at oxygen pressure of 30 mTorr. As a high oxygen pressure will en-

hance the scattering of species in plume and reduce their kinetic energy, it can vary the Li composition in the thin film. Low Li composition in the thin film might cause the suppression of LLT 001 and 003 peaks. From this result, oxygen pressure of 30 mTorr was chose as the optimized condition.

3.3.4 Structure analysis of LLT thin films

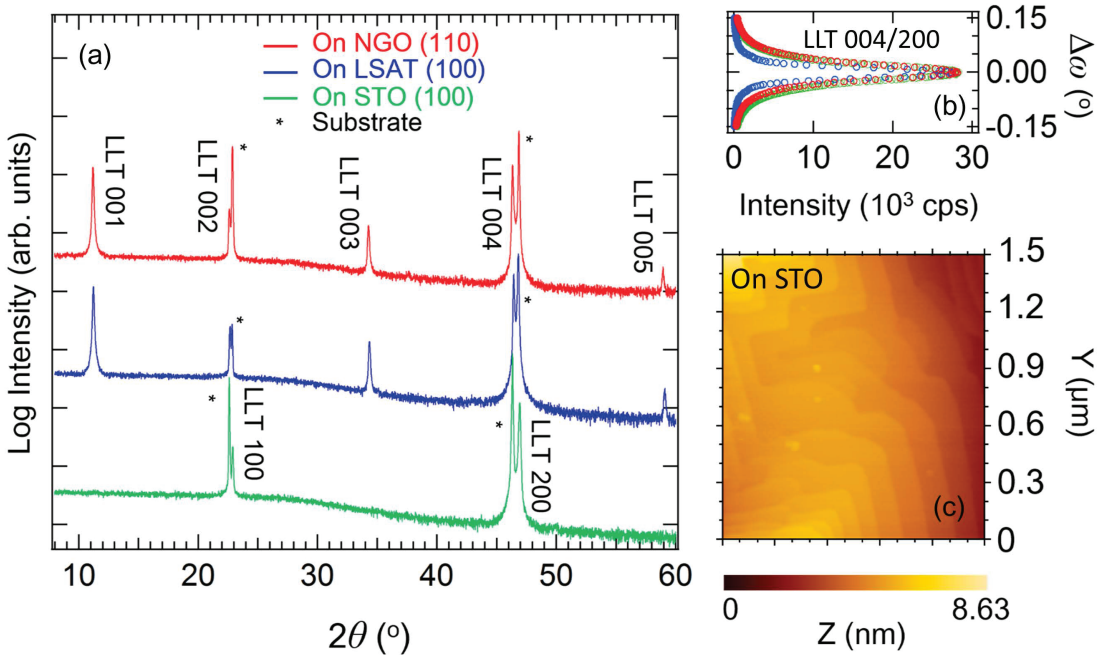

Figure 3.6 (a) Out-of-plane 2θ-θ patterns of 120 nm-thick LLT epitaxial thin films on STO (100) (green), LSAT (100) (blue), and NGO (110) (red) substrate with optimized condition. Asterisks denote peaks from the substrates. (b) Rocking curves of LLT 200 on STO (100) (green), LLT 004 on LSAT (100) (blue), and LLT 004 on NGO (110) (red). (c) Atomic force microscope image of LLT thin film surface on STO (100).

LLT thin films were fabricated on STO (100), LSAT (100) and NGO (110) substrates from a Li-rich $Li_{0.84}La_{0.56}TiO_{3+\delta}$ target at 950 °C with a laser fluence of 1.4 J/cm^2 for 1 h in oxygen pressure of 30 mTorr. The thickness of thin films were 120 nm with a growth rate of 2 nm/min. Figure 3.6 (a) shows the out-of-plane 2θ-θ XRD patterns fabricated at optimized condition on STO (100), LSAT (100) and NGO (110) substrates. Figure 3.6 (b) shows the rocking curve of LLT 200 peak on STO (100) substrate and LLT

004 peaks on LSAT (100) / NGO (110) substrates. The FWHM of these peaks was 0.06°, 0.03° and 0.05°, respectively, representing high crystalline quality of epitaxial LLT thin films. Surface morphology of LLT thin film on step-and-terrace STO (100) substrate is shown in Figure 3.6 (c). The step and terrace structure indicated a layer-by-layer growth mechanism of LLT and high crystalline quality.

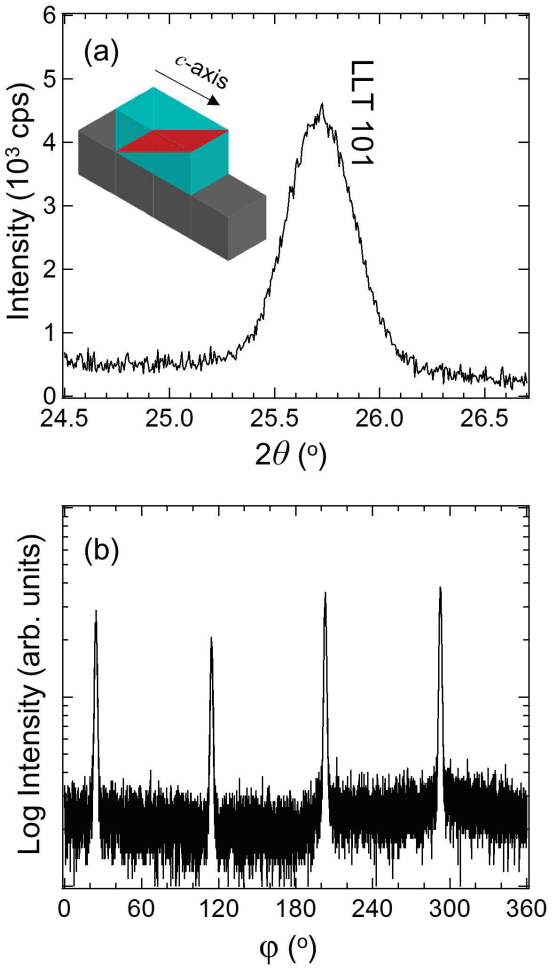

Figure 3.7 (a) 2θ-θ scan for 120 nm-thick LLT 101 peak of epitaxial thin film on STO (100) substrate. (b) Corresponding ϕ-scan for LLT 101 peak.

On STO (100) substrate, the orientation of LLT thin film was along *a*-axis. Figure 3.7 shows the LLT 101 peak in a tetragonal β-LLT phase and its ϕ-scan. From the 4-fold symmetry of LLT 101 peak, it can be derived that the *c*-axis of LLT thin film lay on two directions perpendicular to each other. This indicates that the LLT thin films on

STO (100) have two kinds of in-plane domains with *h*00 orientation.

On LSAT (100) and NGO (110) substrate, the orientations of LLT thin films were along *c*-axis. There was no *c*-axis along in-plane directions observed in these thin films. This indicates that the LLT thin films on LSAT (100) and NGO (110) substrates were single domain structures with 00*l* orientations.

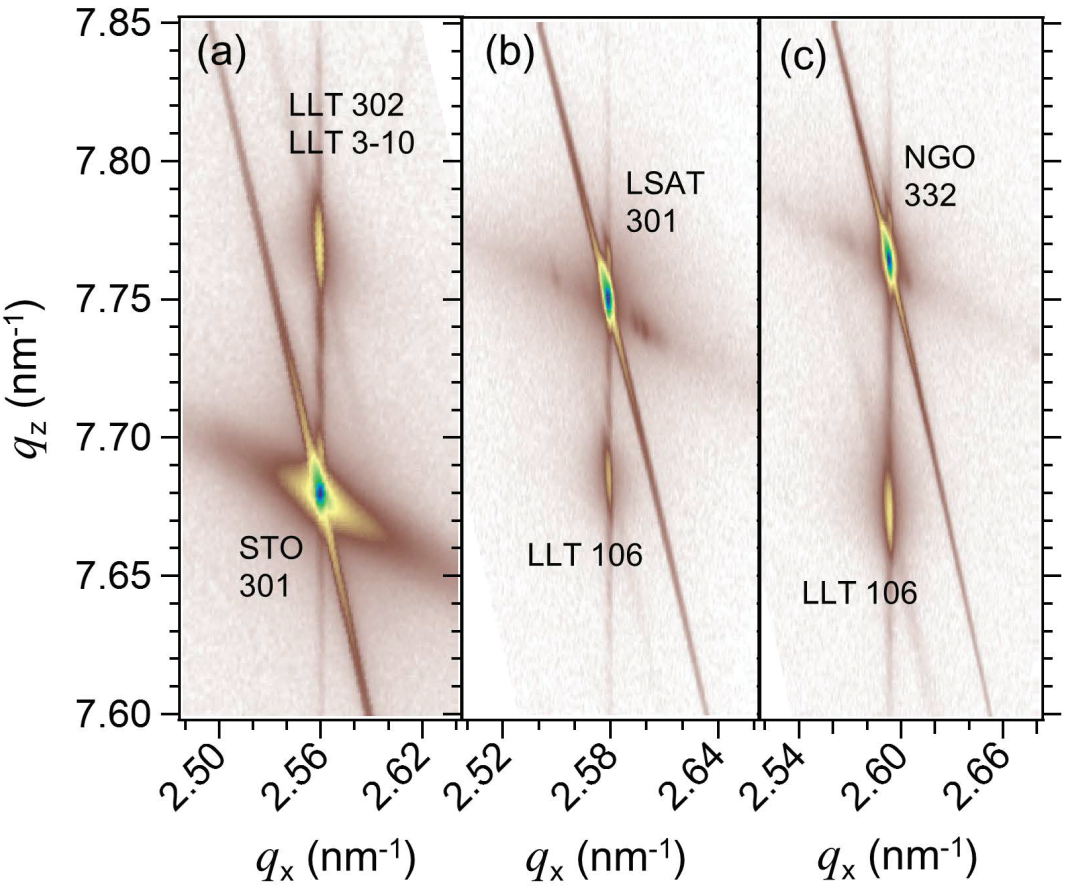

Figure 3.8 Reciprocal space maps of 120 nm-thick LLT thin films on (a) STO (100), (b) LSAT (100), and (c) NGO (110).

Figure 3.8 shows the reciprocal space maps of LLT thin films on different substrates. The in-plane lattice constants of LLT thin films were the same as those of their substrates, showing completely strained lattices. According to these results, the epitaxial relations of LLT thin films and substrates can be determined as

- On STO (100):

  LLT (100) // STO (100), LLT [001] // STO [001] and LLT [001] // STO [010]

- On LSAT (100):

  LLT (001) // LSAT (001), LLT [100] // LSAT [100]

- On NGO (110):

  LLT (001) // NGO (110), LLT [100] // NGO [001] and LLT [010] // NGO [1$\bar{1}$0]

The different orientations of LLT thin films on STO (100) and LSAT (100) / NGO (110) can be explained by lattice strain effect. By comparing the lattice constants of all substrates and LLT, one can find that a_{STO} (a = 0.3905 nm) > $c_{LLT}/2 \geq a_{LLT}/2$ ($a_p \approx$ 0.3875 nm) > a_{LSAT} (a = 0.3868 nm) > $a_{p\ NGO}$ ($a_p \approx$ 0.386 nm). This means that tensile strain was applied on STO substrates while compressive strain was applied on LSAT and NGO substrates. When tensile strain was applied on LLT lattice, *ac*-plane had a smaller lattice mismatch along the in-plane direction, so that it showed *h*00 orientation of LLT with two different kinds of *c*-axis in the in-plane direction on STO (100) substrates. On the other hand, compressive strain on LLT lattice resulted in a smaller mismatch in *ab*-plane along the in-plane direction, so that it showed 00*l* orientation on LSAT (100) and NGO (110) substrates. Figure 3.9 (a) and (b) shows the schematic figure of orientations related to the strain types. These results indicate that the orientation can be controlled by epitaxial strain.

Figure 3.9 (c) shows the calculated lattice parameters and cell volumes of LLT thin films on all substrates according to out-of-plane 2θ-θ scan and reciprocal space mapping. The variable range of LLT lattice parameters is much wider than that of bulk LLT adjusted by Li composition, ranged from 0.3872 to 0.3877 nm [36]. This result indicates that LLT lattice is very flexible against epitaxial strain, and the epitaxial strain can effectively

alternate the bottleneck size for Li hopping instead of chemical and static pressure. Also, the distortion of LLT on orthorhombic NGO (110) substrates was anisotropic along the in-plane directions. The orthorhombically distorted LLT is expected to show anisotropic ionic conductive behavior due to its inequivalent bottleneck.

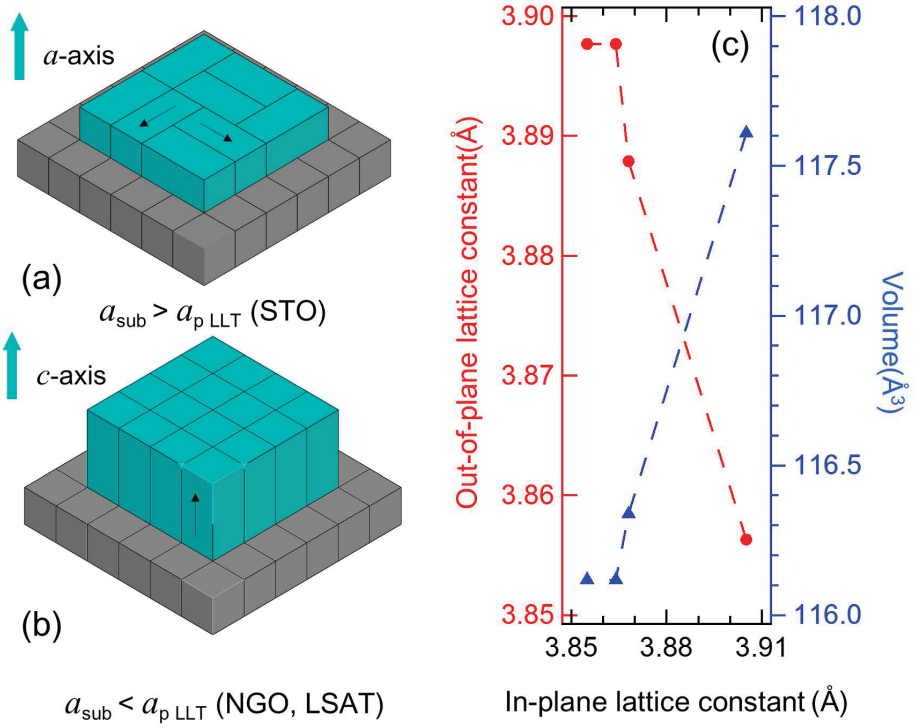

Figure 3.9 Schematic orientation for LLT thin films (green) on different substrates (grey) with (a) tensile strain and (b) compressive strain. (c) Out-of-plane lattice constant (left axis, red) and cell volume calculated as tetragonal perovskite structure (right axis, blue) as a function of in-plane lattice constant of epitaxial LLT thin film on each substrate.

3.3.5 Composition analysis of LLT thin films

Sample preparation

LLT thin film was fabricated on 10×10 mm^2 NGO (110) substrate with thickness of 120 nm. The thin film along with substrate was put in a mixture of 2 mL of 60% HNO_3 and 3 mL of 35% HCl in a Teflon tube. The tube was heated in an oil bath at 100 °C. Figure 3.10 shows the out-of-plane 2θ-θ pattern of LLT thin film after different period of dissolving. After 90 mins heating in the acid mixture, LLT thin film was totally

dissolved. The solution was diluted into 100 mL by ultrapure water as a spectrometry sample solution.

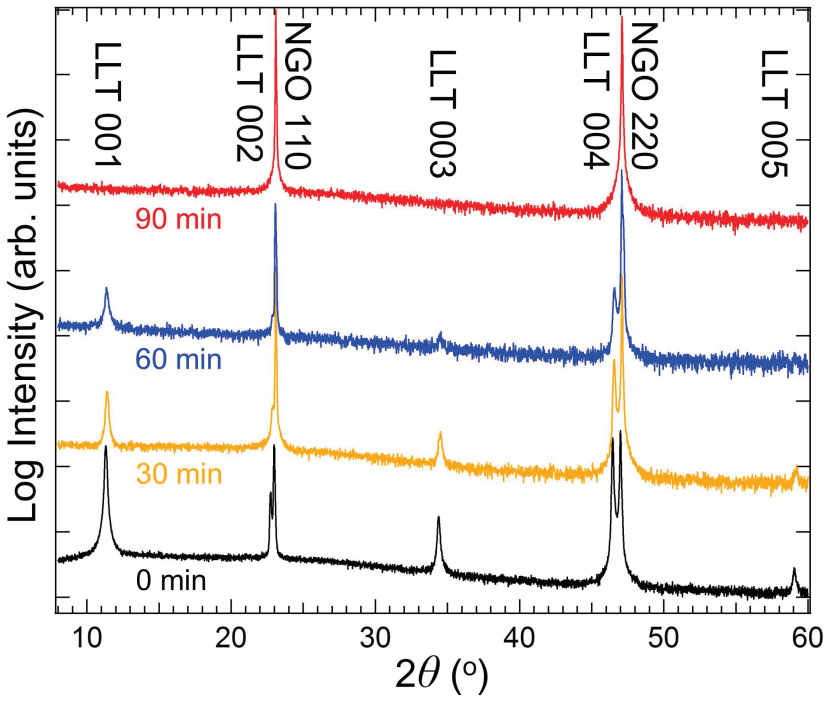

Figure 3.10 Out-of-plane 2θ-θ patterns of 120 nm-thick LLT epitaxial thin films on NGO (110) treated by a mixture of 2 mL of 60% HNO_3 and 3 mL of 35% HCl at 100 °C for different periods of time.

Standard preparation

Standard solutions of La, Ti and Li, as listed in Table 3.1, were prepared by diluting corresponding as-purchased primary standard solutions by ultrapure water. Each standard solution contained 2 mL of 60% HNO_3 and 3 mL of 35% HCl per 100 mL.

Table 3.1 Concentrations of standard solutions

Element	Concentration of Standard (μg/L)			
	No.1	No.2	No.3	No.4
Li	4.51	7.50	14.04	15.04
La	0	300.6	501.0	1002
Ti	0	150.2	250.2	500.5

ICP-OES analysis for La and Ti

ICP-OES was performed to determine La and Ti concentrations in sample solutions. La 412.323 nm and Ti 323.452 nm were chosen as analytical lines. The calibration curves obtained by linear fitting are shown in Figure 3.11. The concentrations of La and Ti were determined as 253 μg/L and 162 μg/L, respectively.

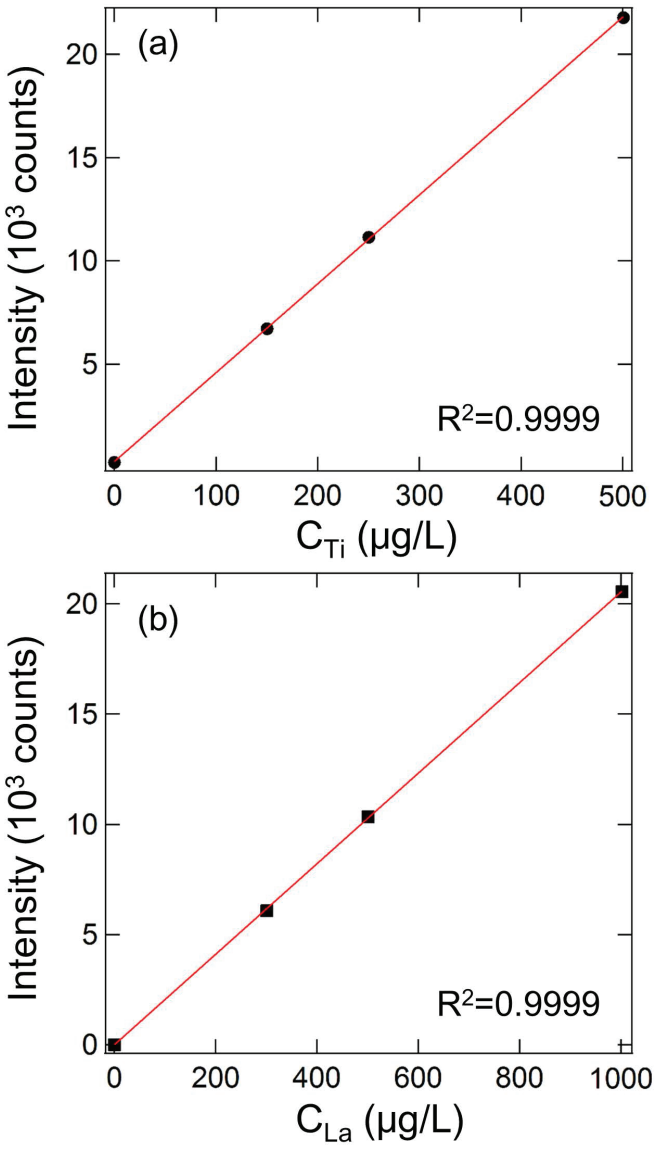

Figure 3.11 Calibration of standard curve obtained by linear fitting of ICP-OES measurement for (a) Ti and (b) La.

GFAAS analysis for Li

GFAAS analysis was performed to determine Li concentration. A 670.8 nm lamp was used as an absorption source. The calibration curve obtained by linear fitting is shown in Figure 3.12. The non-zero intercept at extrapolation of 0 μg/L may due to the instrumental background. The concentration of Li was determined as 7.56 μg/L.

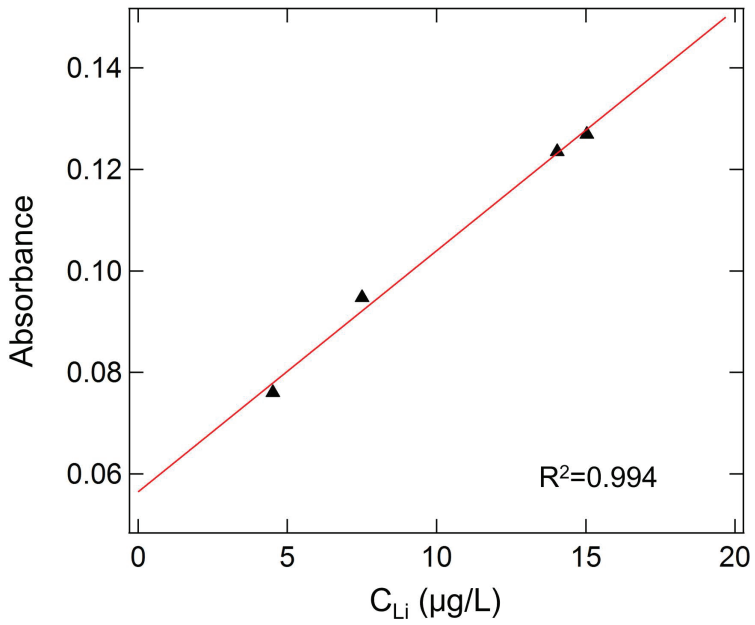

Figure 3.12 Calibration of standard curve obtained by linear fitting of GFAAS measurement for Li.

According to the atomic weight of each element, the molar ratio can be calculated as Li: La: Ti = 0.32: 0.54 : 1. That is, the composition of LLT thin films growth on NGO (110) substrate is determined as $Li_{0.32}La_{0.54}TiO_3$, approximately the same as stoichiometric $Li_{0.33}La_{0.56}TiO_3$. This result indicates that significant loss of Li was seen during PLD process.

3.3.6 Ionic conductivity analysis of LLT thin films

Electrode preparation

Four comb electrodes were patterned as illustrated in Figure 3.13 by photolithography process on LLT thin films on various substrates with 10 × 10 mm^2 areas. Each electrode had a total comb length of 5900 μm and a gap width of 20 μm. 20 nm-thick Ti and 200 nm-thick Au were deposited on photoresist patterned samples. After removing the remained photoresist, electrodes (such as shown in Figure 3.14) perpendicular to STO [100] and [010], LSAT [100] and [010], NGO [001] and [1$\bar{1}$0] were obtained on the same substrate simultaneously .

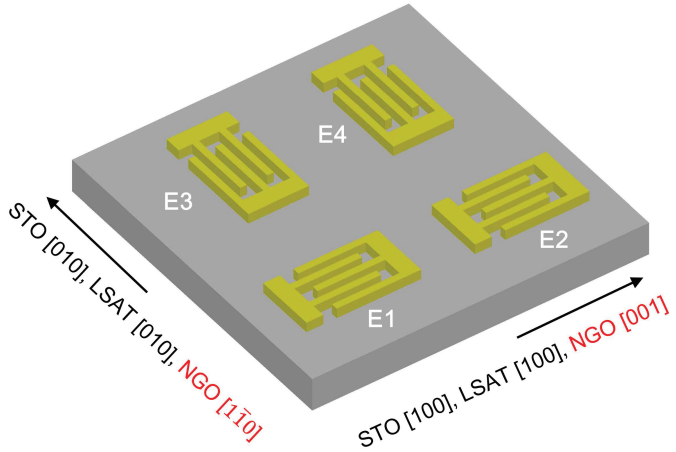

Figure 3.13 Schematic pattern for comb electrodes on LLT thin films.

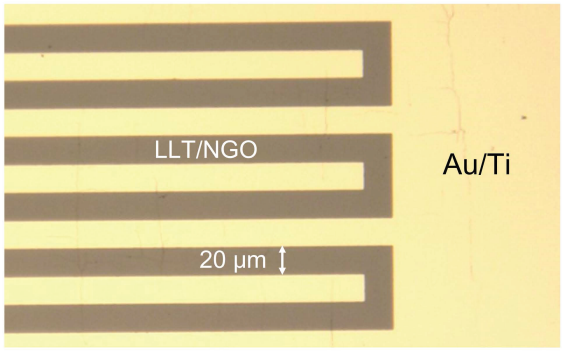

Figure 3.14 Microscopy image for a 5900 μm / 20 μm Au/Ti comb electrode on a LLT thin film grown on NGO (110) substrate.

Temperature stability of electrodes

A 60 nm-thick LLT thin film with prepared electrodes on NGO (110) substrate was preheated at 150 °C for 10 min to remove possible contamination from electrode preparation processes. The sample was cooled down to 25 °C and heated up to 150 °C again for two cycles. Impedance measurements were performed at 40 °C, 50 °C, 60 °C, 70 °C, 80 °C and 90 °C to confirm the temperature stability of the electrodes during measurement.

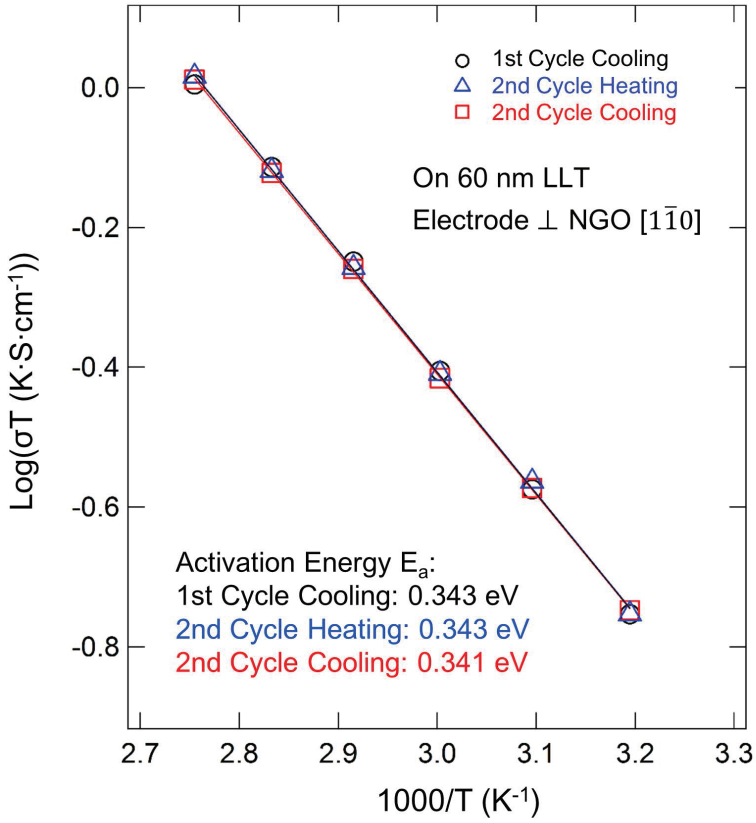

Figure 3.15 Ionic conductivity measured in heating and cooling cycles for a 60 nm-thick LLT thin film fabricated on NGO (110) substrate. The measurements were performed perpendicular to NGO [1$\bar{1}$0] direction.

Figure 3.15 shows ionic conductivity of LLT perpendicular to NGO [1$\bar{1}$0] direction during the heating and cooling cycles. The activation energies calculated from the slope of $\log(\sigma T) - 1000/T$ curves were 0.343, 0.343 and 0.341 eV for the 1st cycle cooling, 2nd cycle heating and 2nd cycle cooling, respectively, with similar ionic conductivity

σ. The consistency of ionic conductivity and activation energy in cooling and heating curves indicates that the electrodes and LLT thin films were stable against heat in air.

Impedance measurement of LLT on NGO substrates

Impedance measurements were performed with an frequency range of 10 Hz - 10 MHz on 120 nm-thick LLT thin film fabricated on NGO (110) perpendicular to NGO [1$\bar{1}$0] and NGO [001] directions after pre-annealing at 150 °C for 10 mins. Here, LLT thin films had the same in-plane lattice constants as their substrates, as shown in Figure 3.8. Thus, LLT thin film was orthogonally distorted in the in-plane direction due to the anisotropic lattice of NGO (110) substrates. The *a*- and *b*- axes of LLT can be defined to be along NGO [001] and NGO [1$\bar{1}$0], respectively, with in-plane lattice constant a_p = 0.3855 nm and b_p = 0.3864 nm. With this definition, in-plane ionic conductivity was measured at the temperature range of 298 - 393 K perpendicular to *a*- and *b*- axes, corresponding to the ionic conduction path across two bottleneck *ac*- and *bc*- planes, respectively.

The epitaxial LLT thin film on NGO substrates showed grain-boundary free ionic conductive behaviour. Figure 3.16 shows the Cole-Cole plots of the LLT thin film measured across *bc*- plane at different temperatures in the frequency range of 10 Hz to 10 MHz. Evidently, these curves showed semicircle type signals at high frequency, finite length diffusion Warburg type signals with 45° slope at medium frequency, and straight lines representing blocking effect of electrode at low frequency. These curves can be simulated by Randle circuit shown in Figure 2.7. The double layer capacitance of simulated Randle circuit across the *bc*- plane of LLT thin film was 3×10^{-12} F at room temperature. Since the double layer capacitances of polycrystalline LLT in bulk researches were in the order of 10^{-9} F for grain-boundary and 10^{-12} F for intra-grain, the impedance response from Figure 3.16 was contributed from intra-grain LLT ionic conductivity and

no grain-boundary signals were observed. As described in Chapter 1, ionic conductivity through grain-boundary in polycrystalline LLT was two orders lower than that of intra-grain. Here, this problem was overcome by high quality boundary-free epitaxial LLT thin films.

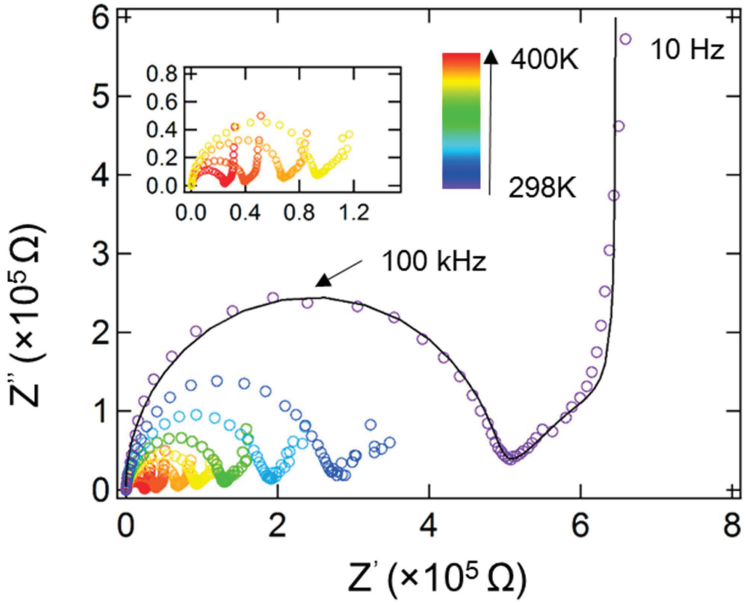

Figure 3.16 Cole-Cole plots of impedance measurement on 120 nm-thick LLT thin film perpendicular to NGO [1$\bar{1}$0] at different temperature. Black line is a fitting curve using Randle circuit shown in Figure 2.7 for room temperature data. Inset shows the enlarged Cole-Cole plots at high temperature.

In-plane anisotropy in ionic conductivity was observed on the LLT thin film on NGO (110) substrates. Figure 3.17 shows the Cole-Cole plots observed for four electrodes with the configuration shown in Figure 3.13 at room temperature. Electrodes E1 and E2 were perpendicular to NGO [001] direction, thus across *ac*-plane, while E3 and E4 were perpendicular to NGO [1$\bar{1}$0], across *bc*-plane. It is clear that the impedance response measured by E1/E2 and E3/E4 are different, which indicates that the ionic conductivity is anisotropic. Essentially the same impedance responses were observed by using two electrodes with the same direction, representing the homogeneity of the thin film and the reproducibility of impedance measurements.

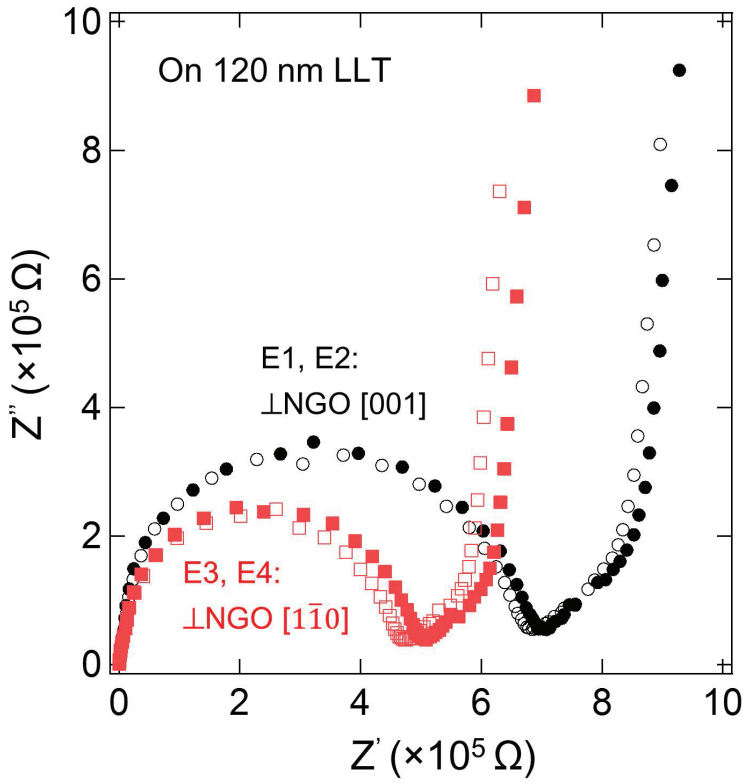

Figure 3.17 Cole-Cole plots of impedance measurement on 120 nm-thick LLT thin film based on electrodes shown in Figure 3.13 perpendicular to NGO [1$\bar{1}$0] and NGO [001] at room temperature temperature.

Figure 3.18 shows the Arrhenius plot of in-plane ionic conductivity of LLT thin film across *ac*- and *bc*- planes. At room temperature, ionic conductivity was 4.3×10^{-4} S·cm^{-1} across *ac*-plane with activation energy of 0.36 eV, while that was 6.7×10^{-4} S·cm^{-1} across *bc*-plane with activation energy of 0.34 eV. Since the lattice constant of bulk cubic $Li_{0.33}La_{0.56}TiO_3$ was evaluted as a_p = 0.3875 nm, the lattice mismatch and compressive strain are larger along *a*-axis than those along *b*-axis in orthorhombically distorted LLT thin films on NGO (110) (see inset of Figure 3.18). Therefore, the bottleneck size for Li hopping path of ionic conduction across *ac*-plane is smaller than that across *bc*-plane. This indicates that lower ionic conductivity with higher activation energy was the consequence of the larger compressive strain due to more contracted bottleneck size. These results are consistent with those of the previous study using static

physical pressure and chemical substitution [42].

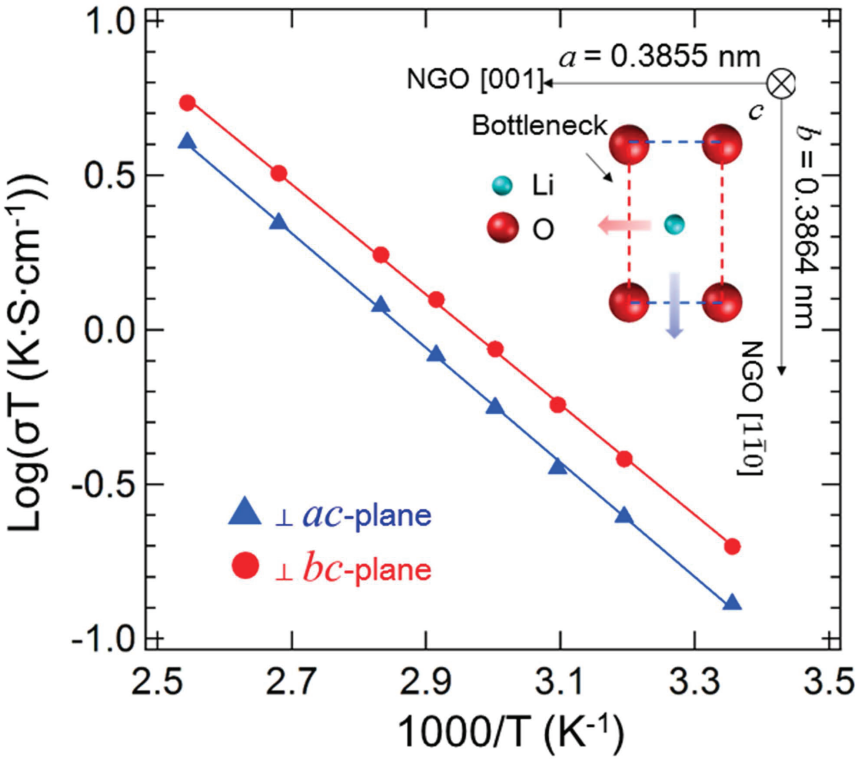

Figure 3.18 Arrhenius plot of in-plane ionic conductivity of 120 nm-thick LLT thin film across *ac*- and *bc*-planes. Inset shows schematic of Li ionic conduction across each bottleneck.

Such biaxial strain is considered to have a larger effect on activation energy than isotropic static pressure. The elasticity equation is described as

$$Y = \frac{\sigma}{\varepsilon} \tag{3.7}$$

$$\varepsilon = (a - a_{\mathrm{p}})/a_{\mathrm{p}} \tag{3.8}$$

where Y is the Young's modulus as $Y = 200$ GPa [76], σ is the equivalent pressure caused by biaxial strain, a is the lattice constant of strained LLT thin film, a_{p} is the original lattice constant of LLT as $a_{\mathrm{p}} = 0.3875$ nm. The equivalent pressure values caused by in-plane biaxial strain along a- and b-axes are calculated as 1.03 GPa and 0.57 GPa, respectively, in LLT on NGO (110) substrates. The relative change of activation energy under pressure $(1/E_{\mathrm{a}}) \cdot (dE_{\mathrm{a}}/dP)$ is 12 %/GPa for biaxial strain, which is almost twice as large as that

for isotropic static pressure in bulk study [42]. It is possible that the total strain of lattice on all the directions was released along the out-of-plane direction under biaxial in-plane strain, while isotropic static pressure was applied on all the directions and cannot be released. Therefore the change of in-plane lattice constant with the same pressure under biaxial strain is larger, and a more contracted bottleneck was obtained due to the larger lateral compression, resulting in the stronger effect on activation energy of LLT.

Impedance measurement of LLT on STO and LSAT substrates

Although anisotropic ionic conductivity was observed with LLT on NGO (110) substrates, there are still more unsolved issues in this field. Instead of compressive strain applied on NGO substrates, tensile strain was also successfully applied to LLT thin film by using larger lattice constant STO substrates. From a simple model, lower activation energy was expected due to the expanded bottleneck. Here, in-plane ionic conductivity measurement was performed with LLT on STO and LSAT substrates.

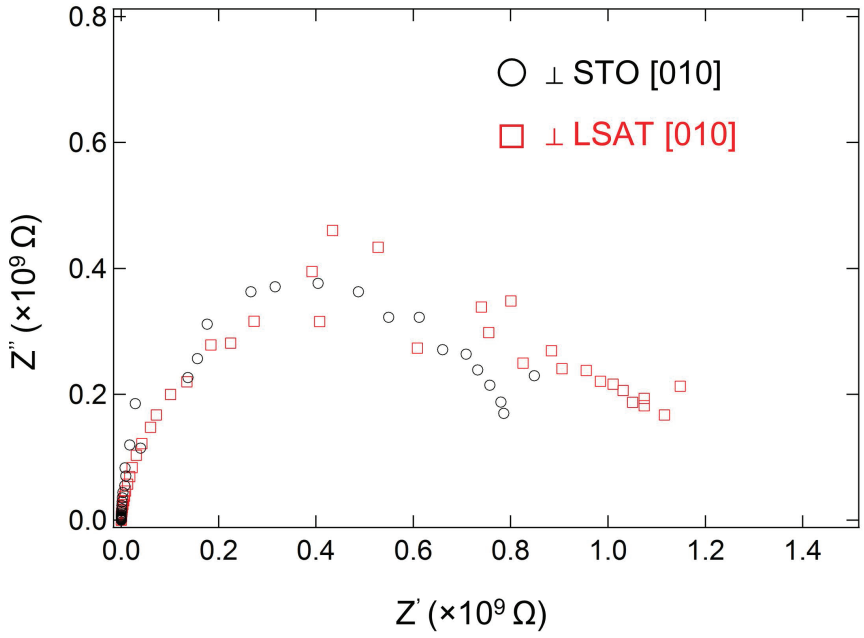

Figure 3.19 Cole-Cole plots of impedance measurements on 120 nm-thick LLT thin film perpendicular to STO [010] and LSAT [010] directions.

Impedance measurements were performed with frequency ranging from 10 Hz to 10 MHz perpendicular to STO [010] and LSAT [010] directions on 120 nm-thick LLT thin films fabricated on STO (100) and LSAT (100). Cole-Cole plots at room temperature are shown in Figure 3.19. As mentioned in Chapter 2, ionic conductive behavior with a blocking electrode can be describe by a Randle circuit shown in Figure 2.7, which yields a semicircle in Cole-Cole plots at high frequency region. However, as shown in Figure 3.19, there was no semicircle type signal at high frequency and the data scattered at low frequency. This indicates that the impedance measurements on LLT with STO and LSAT substrate were not successful. These results were similar to those previously reported for LLT epitaxial thin films on STO (100) substrates [54], where it was suggested that a thin conducting layer formed near the surface of STO substrate under reductive fabrication condition hindered the impedance measurements. However, this cannot explain why the similar phenomenon happened on insulating LSAT substrate. Here, I propose a new model related to LLT-substrate interface, which will be discussed in Chapter 4 of this dissertation.

3.4 Summary and conclusion

In this chapter, high quality $Li_{0.33}La_{0.56}TiO_3$ epitaxial thin films were successfully fabricated by PLD on STO (100), LSAT (100) and NGO (110) substrates. By varying laser fluence in PLD process, Li-loss during fabrication was precisely controlled. Li-composition in the thin film increased with a decreasing laser fluence. With a Li-rich target, phase pure LLT thin films with a high growth rate of 2 nm/min and stoichiometric composition were obtained.

Strain-controlled effects on LLT crystal structure were investigated on LLT epitaxial thin films. By altering the type of in-plane strain, the orientation of LLT thin films was

controlled: *a*-axis orientation with two kinds of in-plane domains perpendicular to each other on STO (100) substrate, and *c*-axis oriention with single domain on LSAT (100) and NGO (110) substrates.

The ionic conductivity in epitaxial thin films was comparable to the intra-grain ionic conductivity in polycrystalline specimens, but did not contain the low grain-boundary conductivity which suppressed the total ionic conductivity in polycrystalline bulk study. Strain-controlled ionic conductive behavior was observed in LLT on orthorhombic NGO substrate due to the anisotropic distortion of in-plane LLT lattice. At room temperature, LLT thin film on NGO (110) substrate had in-plane ionic conductivity of 6.7×10^{-4} $S \cdot cm^{-1}$ with an activation energy of 0.34 eV perpendicular to NGO $[1\bar{1}0]$ direction, and 4.3×10^{-4} $S \cdot cm^{-1}$ with an activation energy of 0.36 eV perpendicular to NGO [001] direction. The ionic conductivity of LLT thin film decreased with increasing compressive strain. The higher activation energy under more compressive strain implies that a more contracted bottleneck for Li-ion hopping was generated, thus hindered the Li ionic conductivity. This tendency is similar to static pressure effect and chemical substitution effect in bulk research. However, the strain effect is stable in the atmospheric condition. According to these results, epitaxial strain is very effective in controlling Li ionic conduction. Not only the high Li ionic conductivity, but also the strain-controlled Li ionic conductivity provided a new prospect and possibility in developing all epitaxial solid state lithium ion battery by using LLT epitaxial thin film.

4 Heterostructure for $Li_{0.33}La_{0.56}TiO_3$ with conductive bottom electrode

4.1 Introduction

As introduced in Chapter 1, lithium lanthanum titanate $Li_{0.33}La_{0.56}TiO_3$ (LLT) with perovskite structure has attracted great interests for its ionic conductivity as high as 10^{-3} $S{\cdot}cm^{-1}$ order at room temperature and the potential in applications of all solid state Li ion batteries. Most of the studies on LLT have been conducted on polycrystalline specimens to measure its ionic conductivity and microstructure. Recently, several studies on single crystal LLT by using heteroepitaxial growth has been reported. In this work (Chapter 3), epitaxial LLT thin films were successfully fabricated and its strain-controlled ionic conductivivity was observed on NGO (110) substrates.

However, most of the previous reports on epitaxial LLT thin films focused on its in-plane ionic conductivity and few studied the out-of-plane one, which is another important direction of Li diffusion to construct all solid state thin film battery structure. In order to understand ionic conductive behavior of epitaxial LLT thin film along the out-of-plane direction, a conductive bottom electrode/LLT/top electrode heterostructure has to be fabricated.

In this Chapter, I demonstrate an epitaxial heterostructure with various perovskite oxide substrates fabricated by PLD method. A high quality phase pure LLT thin film with a $La_{0.6}Sr_{0.4}MnO_3$ (LSMO) buffer layer was fabricated. X-ray reflectometry (XRR) was performed on LLT thin films with and without LSMO buffer layer to study the interface between LSMO and LLT as well as that between LLT and substrates. The study of interface provides a new prospect to explain why the impedance measurements failed as described in Chapter 3 and helps to construct all epitaxial solid state lithium ion battery.

4.2 Experimental methods

LSMO bottom electrodes were fabricated by PLD with KrF excimer laser (λ = 248 nm, Coherent COMPexPro 50) by a $La_{0.6}Sr_{0.4}MnO_3$ target (Toshima Manufacturing Co. Ltd.). Cubic $SrTiO_3$ (100) (STO: a = 0.3905 nm), cubic $(LaAlO_3)_{0.3}$-$(SrAl_{0.5}Ta_{0.5}O_3)_{0.7}$ (100) (LSAT: a = 0.3868 nm), and orthorhombic $NdGaO_3$ (110) (NGO: a = 0.5431 nm, b = 0.5499 nm, c = 0.771 nm) single crystals were chosen as substrates. As-purchased BHF-treated STO (100) substrates were annealed at 1050 °C for 2 h to obtain a step and terrace surface, while as-purchased LSAT (100) and NGO (110) substrates were annealed at 1000 °C for 2 h to obtain a flatter surface. Ablation frequency was set to 2 Hz with a laser fluence of 2 J/cm^2. Substrate temperature and oxygen pressure were 600 °C and 1 mTorr, respectively. The obtained LSMO thin film was post annealed in air at 1000 °C for 2 h to compensate the oxygen vacancies and to improve its electronic conductivity and crystallinity.

LLT thin films were fabricated on LSMO buffer layer with a $Li_{0.84}La_{0.56}TiO_{3+\delta}$ target by PLD. Laser fluence, deposition time and ablation frequency were 1.4 J/cm^2, 30 min and 10 Hz, respectively, with a substrate temperature of 950 °C and oxygen pressure of 30 mTorr.

Reflection high-energy electron diffraction (RHEED) was performed during the fabrication of LSMO. Crystal structures of LLT/LSMO thin films were analyzed by XRD (D8 Discover, Bruker). Surface morphology was measured by AFM (SPI-4000, Hitachi High Technologies). Film thickness was evaluated by a stylus profilometer (Dektak XT, Bruker). The interface was evaluated by X-ray reflectrometry (XRR). XRR spectra were analyzed and simulated with LEPTOS software package. Impedance measurements were performed by an impedance analyzer (Solatron 1260+1296) with a prober system in air.

4.3 Results and discussions

4.3.1 Fabrication of LSMO buffer electrode

In-situ RHEED pattern of LSMO fabrication

As introduced in Chapter 2, RHEED is a very effective method to perform in-situ monitoring of thin film fabrication. Here, RHEED observation was performed for epitaxial LSMO thin film growth on STO (100), LSAT (100) and NGO (110) substrates.

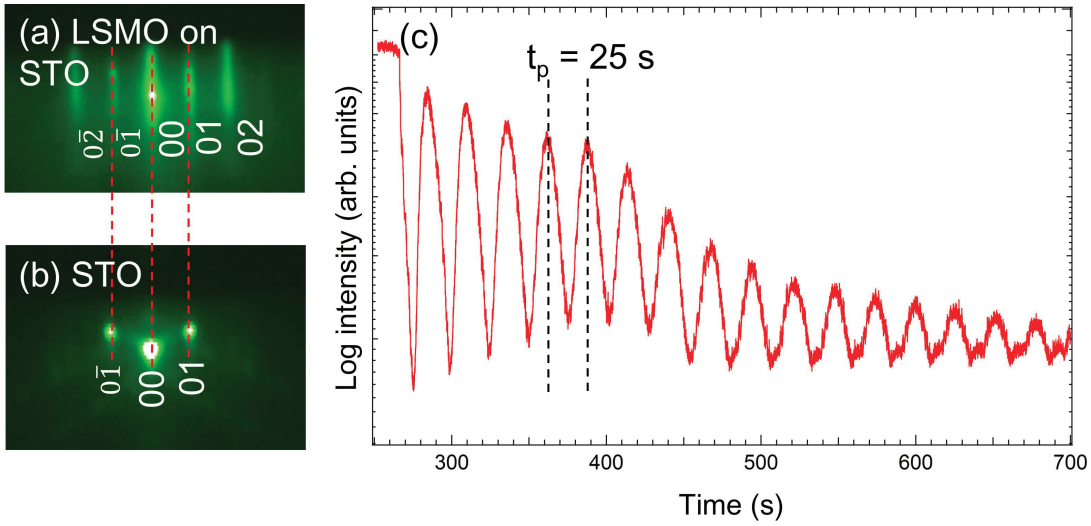

Figure 4.1 RHEED pattern of (a) LSMO layer compared with (b) STO substrate. (c) Peak intensity of LSMO 01 versus time.

Figure 4.1 shows the RHEED pattern and the intensity-time plots for LSMO thin film growth on STO (100) substrate. By comparing the RHEED patterns of STO substrate and LSMO thin film, it is clear that the vertical distance between STO 00 and STO 01 is the same as that between LSMO 00 and LSMO 01. This indicates that LSMO grew coherently with the same lattice constant as STO. Figure 4.1 (c) shows clear oscillation of peak intensity for LSMO 01. This indicates a layer-by-layer growth of LSMO layer on STO substrate. The period of oscillation was about 25 s, representing a cycle to form a LSMO monolayer with a thickness of 0.4 nm, from which the growth rate was estimated as about 0.008 nm/pulse. Therefore, the thickness of LSMO layer deposited for 30 mins

was estimated to be 28 nm, which was consistent with the thickness measured by stylus profilometer.

Post-annealing of LSMO layer

LSMO contains *p*-type carriers so that oxygen vacancies are not preferred for obtaining highly conductive LSMO bottom electrodes. Here, the as-deposited film was annealed in air to compensate the oxygen vacancies generated in PLD process.

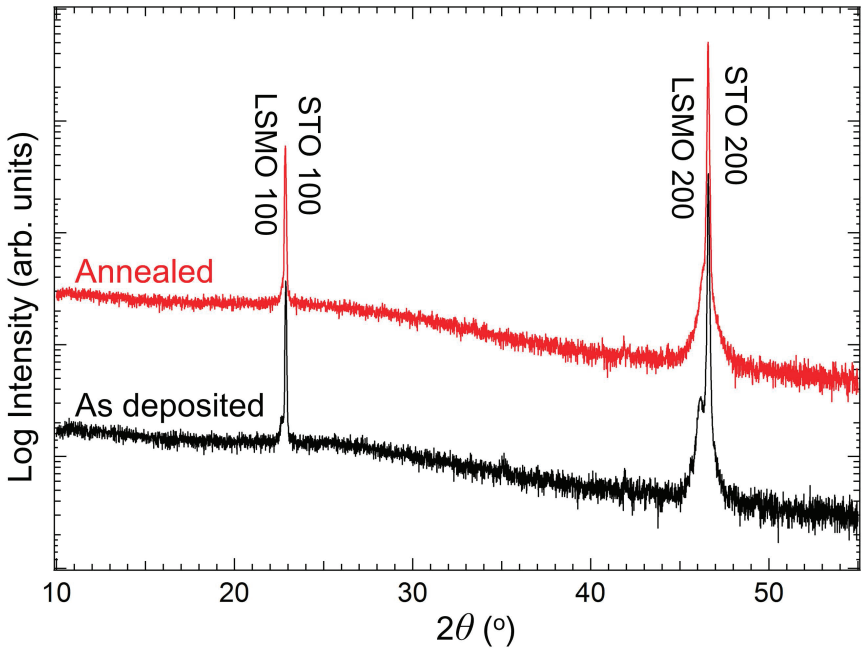

Figure 4.2 Out-of-plane 2θ-θ XRD patterns for as-deposited (black) and annealed (red) LSMO layer on STO (100) substrate.

Figure 4.2 shows the out-of-plane 2θ-θ XRD patterns of LSMO layer before and after annealing. It is clear that the LSMO peaks shifted to the higher angle direction, representing a smaller out-of-plane lattice constant. According to the previous research [77], generation of oxygen vacancies results in expansion of out-of-plane lattice in LSMO epitaxial thin film. Also, the resistance in annealed thin films was two orders lower than that in as-deposited ones measured by a multi-function meter. These results indicate that oxygen vacancies were compensated by the annealing process and a highly conductive

bottom electrode was obtained.

Figure 4.3 shows the surface morphology of annealed LSMO layer on STO substrates. The surface showed step-and-terrace structure, which is consistent with layer-by-layer oscillation observed by RHEED. This atomically flat surface should benefit in a good contact between LSMO bottom electrode and the upper LLT thin film, and could avoid possible electronic leakage during impedance measurement.

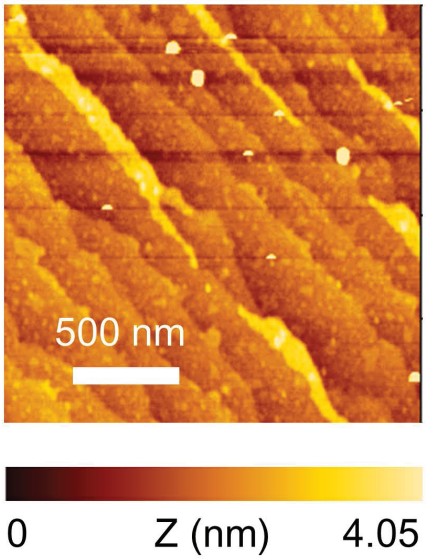

Figure 4.3 AFM image of LSMO layer on STO (100) substrate after annealing in air at 1000 °C for 2 h.

4.3.2 Fabrication of LLT thin films on LSMO bottom electrodes

LLT thin films were fabricated on STO (100), LSAT (100) and NGO (110) substrates with LSMO bottom electrodes. The thickness of the LSMO and LLT layers were 25 nm and 65 nm, respectively. Figure 4.4 shows the out-of-plane 2θ-θ XRD patterns on various substrates. On all the substrates, LSMO had 001 orientation with pseudo-cubic lattice. The LLT thin film on LSMO bottom electrode fabricated on each substrate has the same orientation as LLT fabricated directly on the substrate, which is discussed in Chapter 3. This means that on STO (100), LLT thin film was *a*-axis oriented while on

LSAT (100) and NGO (110), LLT thin films were *c*-axis oriented.

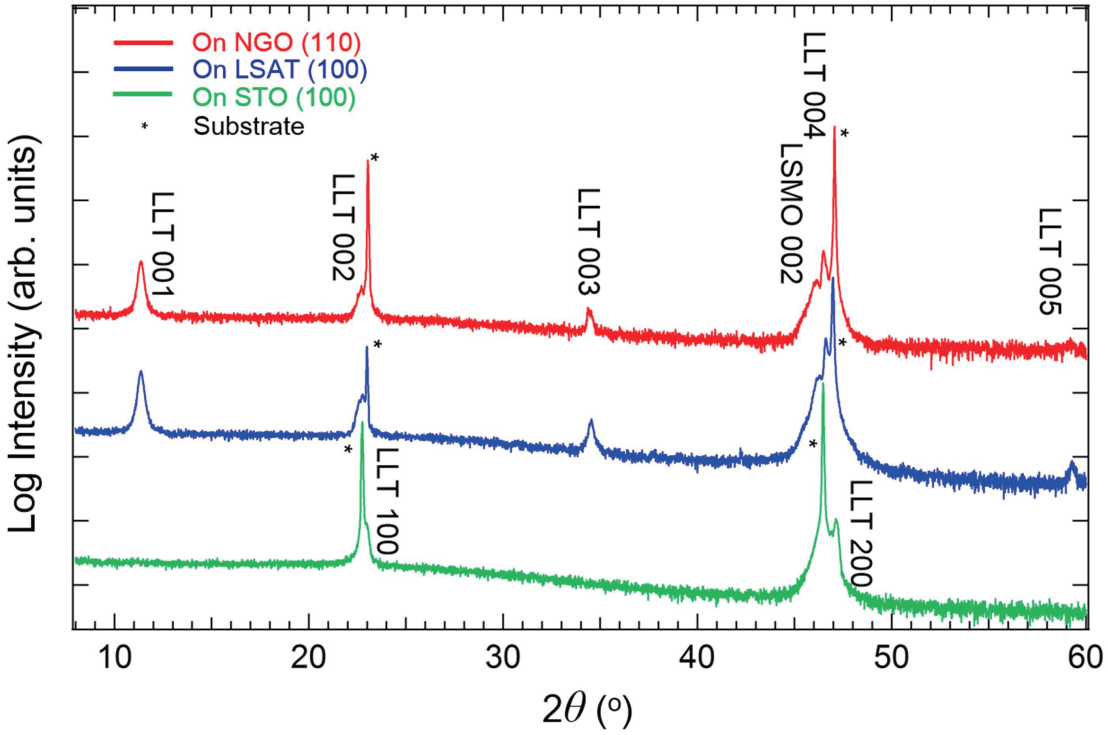

Figure 4.4 Out-of-plane 2θ-θ XRD patterns of LLT/LSMO epitaxial thin films on STO (100) (green), LSAT (100) (blue), and NGO (110) (red) substrate. Asterisks denote peaks from the substrates.

FWHM values of rocking curve for LLT 004 or 200 peaks on STO, LSAT and NGO were 0.07° , 0.06° and 0.06°, respectively. This result represents high crystalline quality of LLT fabricated on LSMO bottom electrode, which also indicates the high crystalline quality of LLT/LSMO heterostructure. Compared these values with that of LLT directly growth on the substrates (0.03°), one can find that the FWHM of LLT/LSMO is slightly larger. It is probably due to the partial relaxation of strain induced by lattice mismatch of LSMO/LLT and LSMO/substrate interfaces.

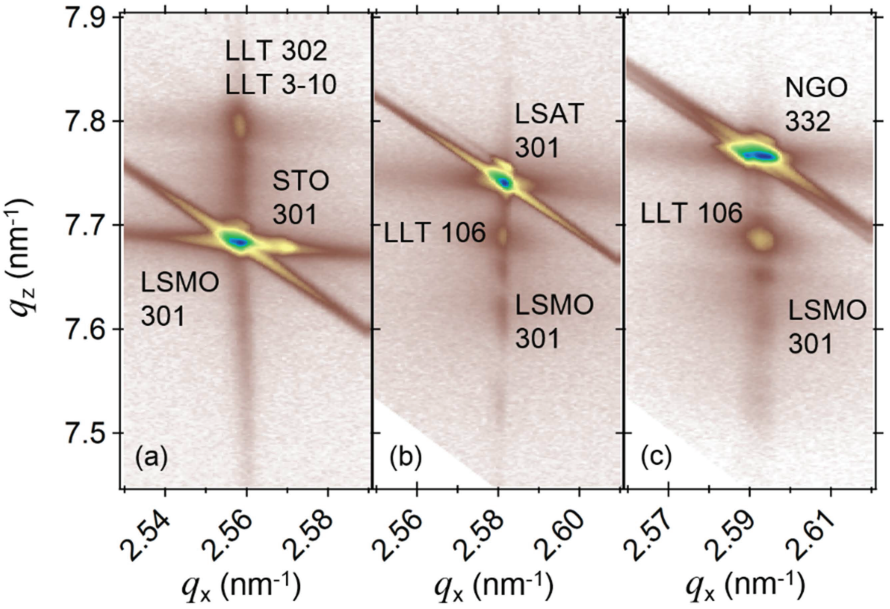

Figure 4.5 Reciprocal space maps of LLT/LSMO epitaxial thin films on (a) STO (100), (b) LSAT (100), and (c) NGO (110).

Figure 4.5 shows the reciprocal space maps of LLT thin films on various substrates with LSMO bottom electrodes. The in-plane lattice constants of LLT thin films were the same as those of their substrates, similar to the LLT thin films directly growth on substrates described in Chapter 3. However, the peaks were broadened in the in-plane direction, representing partially strain-relaxed lattice, resulting in wider FWHM in their rocking curves. According to these results, the epitaxial relations of LLT thin films and substrates can be determined as

- On STO (100):

  LLT (100) // LSMO (001) // STO (100), LLT [001] // LSMO [100] // STO [001] and LLT [001] // LSMO [100] // STO [010]

- On LSAT (100):

  LLT (001) // LSMO (001) // LSAT (001), LLT [100] // LSMO [100] // LSAT [100]

- On NGO (110):

LLT (001) // LSMO (001) // NGO (110), LLT [100] // LSMO [100] // NGO [001] and LLT [010] // LSMO [010] // NGO [1$\bar{1}$0]

4.3.3 Impedance spectra of LLT thin films in out-of-plane direction

LSMO layer was deposited on a 5 × 10 mm^2 substrate and LLT thin film was fabricated on the LSMO layer with an area of 5 × 5 mm^2. The thicknesses of LSMO and LLT layers were 25 nm and 65 nm, respectively. 20 nm-thick Ti and 200 nm-thick Au electrodes were deposited on LSMO and LLT with a circular diameter of 3 mm by UHV evaporation. Impedance measurements were performed in frequency range of 10 Hz - 10 MHz after pre-annealing to 150 °C for 10 mins and cooling down to room temperature.

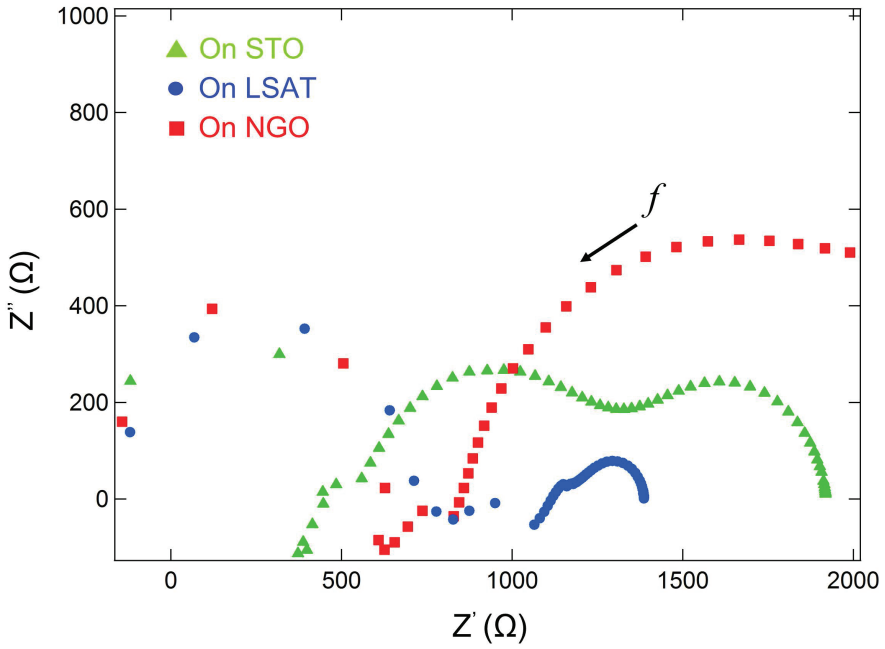

Figure 4.6 Cole-Cole plots of out-of-plane impedance spectra of LLT with LSMO bottom electrode on STO (green), LSAT (blue) and NGO (red).

Figure 4.6 shows the Cole-Cole plots measured on STO (100), LSAT (100) and NGO (110) substrates. It is clear that there are semi-circle type signals in low frequency region with scattered data points at high frequency. However, the double layer capacitance simulated by Randle circuit was of the order of 10^{-7} F, which is too high compared

with the bulk and boundary ionic conductivity in polycrystalline LLT specimens. Also, the spectra contain several semi-circles representing different kinds of charge transfer behaviors in the same sample. It is possible that these signals came from undesired interface layers in the heterostructure.

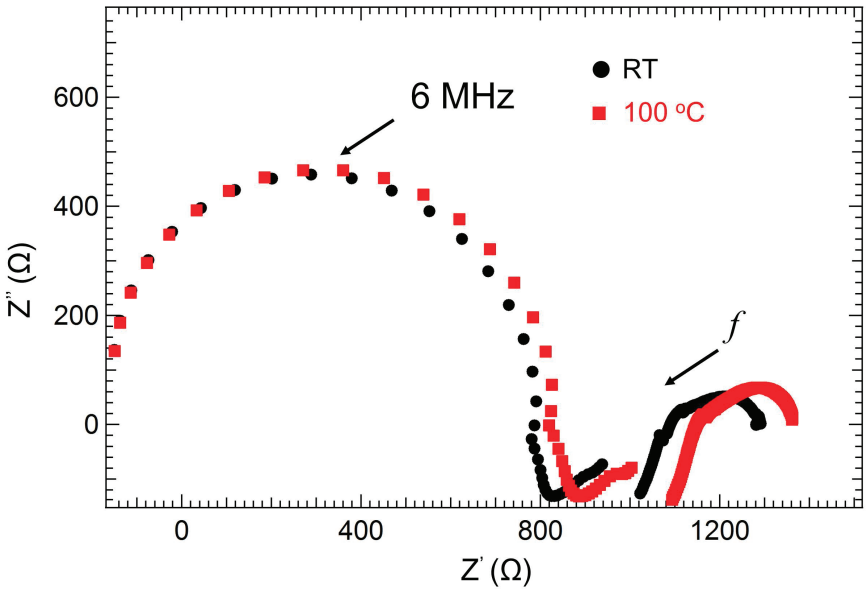

Figure 4.7 Cole-Cole plots of out-of-plane impedance spectra of LLT with LSMO bottom electrode on LSAT measured at room temperature (black) and 100 °C (red).

In order to understand whether these signals belong to ionic conductive behavior, where the diameters of semi-circles indicating charge transfer resistance decrease with increased temperature (see Figure 3.16), impedance measurements were also performed at 100 °C with more sampling points at high frequency on LSAT substrate. Figure 4.7 shows the Cole-Cole plots measured at room temperature and 100 °C. Although there is a semi-circle signal with capacitance of the order of 10^{-11} F order in the high frequency region, the charge transfer resistance tended to increase at high temperature. Therefore, the signals cannot be attributed to ionic conduction of LLT, but might originate from metallic interface or electrodes.

According to the discussion above, the impedance measurement of out-of-plane

direction for LLT thin film was not successful with epitaxial heterostructure. It is possible that the charge transfer resistance of LLT was too small to detect because of the large area of electrodes. Thus micrometer scale electrodes are required in future research, despite the difficulty in electrode preparation and measurement with usual impedance analysis system. However, this cannot explain the multiple semi-circle signals in the impedance spectra in Figures 4.6 and 4.7, which were never found in the in-plane measurements.

4.3.4 Interface study on heterostructure of LLT epitaxial thin film

In order to explain the multiple semi-circle signals in the impedance spectra mentioned above, I inferred that these signals originated from the interfaces in the multi-layer epitaxial heterostructure. Here, XRR measurements were performed on LLT/LSMO/NGO heterostructure in comparison to LLT/NGO system, in which the thickness of LLT was about 60 nm.

Figure 4.8 shows XRR spectra with refined curves and the density profiles for LLT/LSMO and LLT films on NGO (110) substrates. Since LLT was proved to be stochiometric by chemical analysis (Chapter 3), the density of each layer was assumed to be equal to its theoretical value. For LLT/NGO, a two-layer model was adopted. The thickness of LLT thin film was simulated as 63.2 nm and roughness at interface was 1.5 nm, with a residual sum of squares (RSS) of 0.002. For LLT/LSMO/NGO, a three-layer model was used. The thicknesses of LSMO and LLT layers were 22.3 nm and 64.5 nm, respectively, with a RSS of 0.005. The roughness values of LSMO/NGO and LLT/LSMO interface were 1.4 nm and 6.7 nm, respectively. This result indicates that there is a much thicker interface region between LSMO and LLT layers compared with LLT/NGO and LSMO/NGO interfaces.

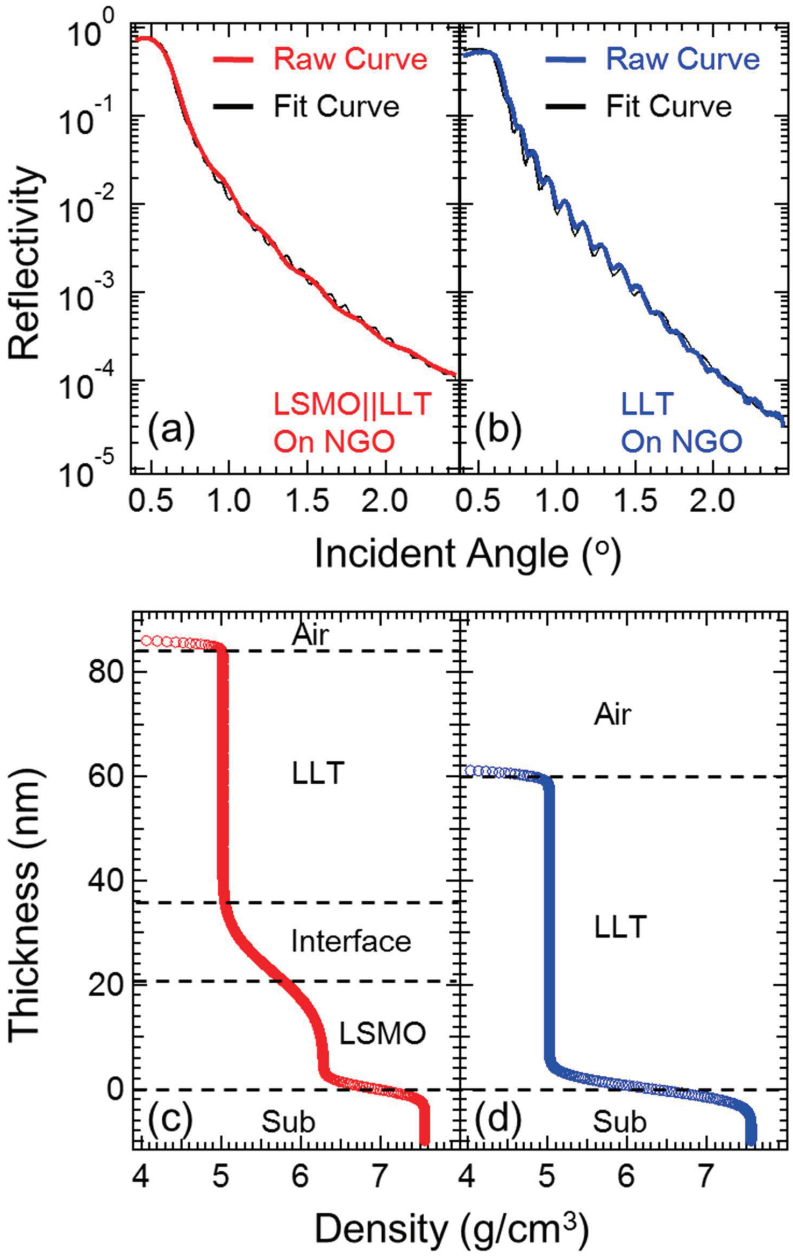

Figure 4.8 X-ray reflection spectra and density profiles of LLT with LSMO bottom electrodes(a, c) and LLT (b, d) thin film on NGO (110) substrate.

The roughness of LLT/LSMO interface is similar to that of LLT/STO and LLT/LSAT interfaces. Figure 4.9 shows XRR spectra with refined curves and the density profiles for LLT/STO, LLT/LSAT and LLT/NGO systems. All the systems were simulated by a two-layer model. On STO substrate, the thickness of LLT thin film was simulated as 60.8 nm with a interface roughness of 6.7 nm, and the thickness of LLT on LSAT substrate was

60.2 nm with a interface roughness of 6.1 nm. Notably, the roughness of the interface between LLT and STO/LSAT is much larger than that of LLT/NGO interface, and is similar to that of LLT/LSMO interface.

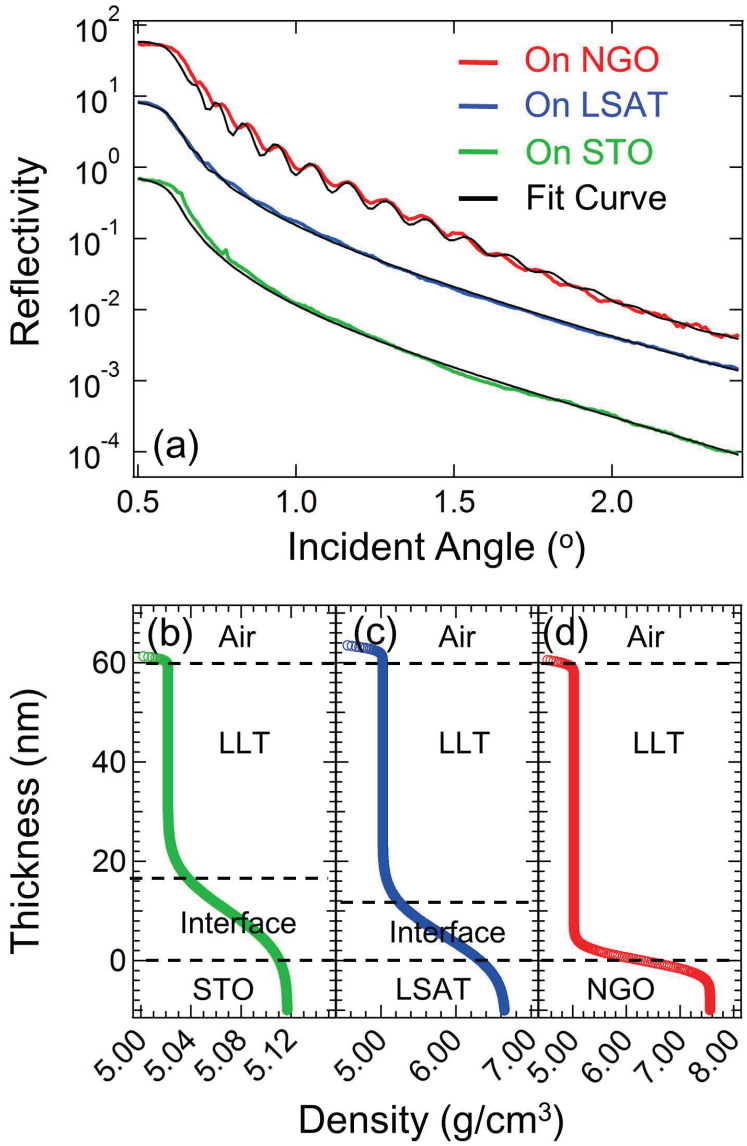

Figure 4.9 (a) X-ray reflection spectra of LLT on STO (green), LSAT (blue) and NGO (red) substrates with fitting curves (black). The data was shifted vertically for convenience. Density profiles for LLT on (b) STO, (c) LSAT and (d) NGO.

As discussed in Chapter 3, the in-plane ionic conductivity was not measured successfully on LLT/LSAT and LLT/STO, and this cannot be explained by substrate reduction. As described in this chapter, the out-of-plane impedance spectrum with LSMO

bottom electrode also showed unknown charge transfer behavior which cannot be attributed to ionic conductivity. Considering the results of interface XRR studies on these heterostructures, it is suggested that these abnormal signals in impedance spectra are related to the rough interface structures. Regarding the similarity of LLT/LSAT, LLT/STO and LLT/LSMO, the rough interface is probably due to Sr-La intermixing because all structures contain Sr. Sr-La intermixing has been investigated in many perovskite heterostructures, such as $LaAlO_3/SrTiO_3$ [78] and $LaMnO_3/SrMnO_3$ [79]. The intermixing was considered as the result of similar ionic radius of Sr^{2+} and La^{3+} as well as the instability of surface dipole energy. Sr-La intermixing may occur more easily in LLT than in normal perovskites, because LLT contains a certain amount of A-site vacancies intrinsically. Sr^{2+} from LSMO layer and STO/LSAT substrates can easily diffuse into LLT via the vacancies under high growth temperature. This might result in the rough interfaces at LLT/LSMO, LLT/LSAT and LLT/STO. On the other hand, on Sr-free NGO substrate, the LLT/NGO interface was much sharper, so that the in-plane ionic conductivity was measured successfully.

4.4 Summary and conclusion

In this chapter, I successfully fabricated high quality $Li_{0.33}La_{0.56}TiO_3$ epitaxial thin films on $La_{0.6}Sr_{0.4}MnO_3$ bottom electrodes on STO (100), LSAT (100) and NGO (110) substrates by PLD. The orientations and lattice constants of LLT thin films on LSMO bottom electrodes were similar to those of LLT epitaxial thin films discussed in Chapter 3. This indicates that LSMO/LLT heterostructure is a promising structure to study the out-of-plane ionic conductive behavior under substrate strains.

LLT/LSMO interface was found to be rough and similar to LLT/LSAT and LLT/STO interfaces, probably due to Sr-La intermixing. The LSMO/LLT interface may have d-

ifferent composition and properties from bulk LLT, which would largely contribute to the abnormal charge transfer signals. Therefore, in order to investigate the out-of-plane ionic conductive properties by using LSMO/LLT heterostructure, more studies on the interfaces should be done by using microscopic measurements and precise impedance analysis with micro electrodes.

Strained and conductive LSMO buffered LLT demonstrated in this chapter would provide a new prospect to study the intrinsic ionic conductive behavior under strain. This would also help us to construct the foundation toward all epitaxial solid state lithium ion battery structure in the future research.

5 General conclusion

In this dissertation, solid state Li-ion conductor $Li_{0.33}La_{0.56}TiO_3$ (LLT) epitaxial thin film was fabricated by PLD method and its ionic conductive properties were characterized. Epitaxial heterostructure using LLT and $La_{0.6}Sr_{0.4}MnO_3$ (LSMO) bottom electrode was also fabricated successfully. The interfaces of the heterostructures were investigated in detail by XRR.

Thin film growth of $Li_{0.33}La_{0.56}TiO_3$ and strain-controlled ionic conductivity

LLT thin films were successfully fabricated by PLD method on perovskite substrates STO (100), LSAT (100) and NGO (110) which have different lattice constants. The Li-composition in the thin film was found to be higher at lower laser fluence in PLD process. A Li-rich target was used to obtain high quality phase pure LLT epitaxial thin films with stoichiometric composition. The orientation and lattice constant of LLT were controlled by epitaxial strain. In-plane ionic conductivity was successfully measured and was comparable to the bulk one, without observing low boundary conductivity as seen in polycrystalline LLT.

Strain-controlled ionic conductive behavior was observed on LLT fabricated on orthorhombic NGO (110) substrate due to the anisotropic distortion in the in-plane direction. Larger compressive in-plane strain resulted in a more contracted bottleneck for Li-ion hopping. Lower ionic conductivity and higher activation energy were observed across the more contracted bottleneck. Different from the similar tendency in static pressure and chemical substitution effect studied by bulk specimens, the strain effects in epitaxial thin films are stable in the atmospheric condition.

Heterostructure for $Li_{0.33}La_{0.56}TiO_3$ with conductive bottom electrode

High quality LLT epitaxial thin films with LSMO bottom electrodes on STO (100), LSAT (100) and NGO (110) substrate were fabricated by PLD to investigate the out-of-plane ionic conductive properties. Although the ionic conductivity was not successfully measured, the results of XRR measurements indicated that there was rough interface between LLT and LSMO layers. This interface was similar to that between LLT and LSAT and between LLT and STO, possibly due to the Sr-La intermixing phenomenon. In order to investigate the out-of-plane ionic conductive properties by using LSMO/LLT heterostructure, more studies on the interfaces should be done in the future research.

Future prospects

This dissertation proved that epitaxial strain is an effective way to control the ionic conductivity of LLT, providing a new aspect to achieve strain engineering of LLT solid Li-ion conductor. The heterostructure with bottom electrode provided a preliminary structure toward battery. By fabricating epitaxial cathode and anode layers, all solid state epitaxial Li-ion battery can be constructed for potential applications in micro devices.

In conclusion, this dissertation investigated the Li-ion conductor LLT epitaxial thin films. Systematic researches on thin film fabrication enabled to obtain single crystal LLT in high quality epitaxial thin film form. Strain-controlled ionic conductive properties were studied for the first time, indicating the possibility to improve the ionic conductive properties artificially. Heterostructures with bottom electrodes were fabricated, paving the way for all solid state lithium ion batteries with epitaxial LLT Li-ion conductor.

References

[1] F. Gamble, J. Osiecki, M. Cais, R. Pisharody, F. DiSalvo, T. Geballe, *Science* **174**, 493 (1971).

[2] M. S. Whittingham, *Science* **192**, 1126 (1976).

[3] M. S. Whittingham. Rechargeable electrochemical cell with cathode of stoichiometric titanium disulfide (1978). US Patent 4,084,046.

[4] M. S. Whittingham. Chalcogenide battery (1977). US Patent 4,009,052.

[5] K. Mizushima, P. Jones, P. Wiseman, J. Goodenough, *Solid State Ionics* **3**, 171 (1981).

[6] R. Yazami, P. Touzain, *Journal of Power Sources* **9**, 365 (1983).

[7] A. Yoshino, K. Sanechika, T. Nakajima. Secondary battery (1987). US Patent 4,668,595.

[8] Sony Energy Devices Corporation. Keywords to understanding sony energy devices, http://www.sonyenergy-devices.co.jp/en/keyword/.

[9] R. J. Brodd, *Batteries for Sustainability: Selected Entries from the Encyclopedia of Sustainability Science and Technology* (Springer Science & Business Media, 2012).

[10] W. Van Schalkwijk, B. Scrosati, *Advances in Lithium-Ion Batteries* (Springer Science & Business Media, 2002).

[11] V. Etacheri, R. Marom, R. Elazari, G. Salitra, D. Aurbach, *Energy & Environmental Science* **4**, 3243 (2011).

[12] J.-M. Tarascon, M. Armand, *Nature* **414**, 359 (2001).

[13] D. Aurbach, *Nonaqueous Electrochemistry* (CRC Press, 1999).

[14] K. Kumai, H. Miyashiro, Y. Kobayashi, K. Takei, R. Ishikawa, *Journal of Power Sources* **81**, 715 (1999).

[15] J. Song, Y. Wang, C. Wan, *Journal of Power Sources* **77**, 183 (1999).

[16] A. M. Stephan, *European Polymer Journal* **42**, 21 (2006).

[17] G. Pistoia, *Lithium-Ion Batteries: Advances and Applications* (Newnes, 2013).

[18] J. F. Oudenhoven, L. Baggetto, P. H. Notten, *Advanced Energy Materials* **1**, 10 (2011).

[19] N. Kamaya, K. Homma, Y. Yamakawa, M. Hirayama, R. Kanno, M. Yonemura, T. Kamiyama, Y. Kato, S. Hama, K. Kawamoto, *et al.*, *Nature Materials* **10**, 682 (2011).

[20] Y.-F. Y. Yao, J. Kummer, *Journal of Inorganic and Nuclear Chemistry* **29**, 2453 (1967).

[21] B. Boukamp, R. Huggins, *Physics Letters A* **58**, 231 (1976).

[22] U. v. Alpen, A. Rabenau, G. Talat, *Applied Physics Letters* **30**, 621 (1977).

[23] V. Thangadurai, A. K. Shukla, J. Gopalakrishnan, *Journal of Material Chemistry* **9**, 739 (1999).

[24] H.-P. Hong, *Materials Research Bulletin* **13**, 117 (1978).

[25] J. Bates, N. Dudney, G. Gruzalski, R. Zuhr, A. Choudhury, C. Luck, J. Robertson, *Solid state ionics* **53**, 647 (1992).

[26] F. Mizuno, A. Hayashi, K. Tadanaga, M. Tatsumisago, *Advanced Materials* **17**, 918 (2005).

[27] K. Takada, N. Aotani, S. Kondo, *Journal of Power Sources* **43**, 135 (1993).

[28] R. Kanno, M. Murayama, *Journal of The Electrochemical Society* **148**, A742 (2001).

[29] Y. Inaguma, C. Liquan, M. Itoh, T. Nakamura, T. Uchida, H. Ikuta, M. Wakihara, *Solid State Communications* **86**, 689 (1993).

[30] V. Thangadurai, H. Kaack, W. J. Weppner, *Journal of the American Ceramic Society* **86**, 437 (2003).

[31] J. Haruyama, K. Sodeyama, L. Han, K. Takada, Y. Tateyama, *Chemistry of Materials* **26**, 4248 (2014).

[32] S. P. Ong, Y. Mo, W. D. Richards, L. Miara, H. S. Lee, G. Ceder, *Energy & Environmental Science* **6**, 148 (2013).

[33] Y. Harada, Y. Hirakoso, H. Kawai, J. Kuwano, *Solid State Ionics* **121**, 245 (1999).

[34] Y. Harada, T. Ishigaki, H. Kawai, J. Kuwano, *Solid State Ionics* **108**, 407 (1998).

[35] T. Okumura, T. Ina, Y. Orikasa, H. Arai, Y. Uchimoto, Z. Ogumi, *Journal of Materials Chemistry* **21**, 10195 (2011).

[36] Y. Inaguma, M. Itoh, *Solid State Ionics* **86**, 257 (1996).

[37] X. Gao, C. A. Fisher, T. Kimura, Y. H. Ikuhara, A. Kuwabara, H. Moriwake, H. Oki, T. Tojigamori, K. Kohama, Y. Ikuhara, *Journal of Materials Chemistry A* **2**, 843 (2014).

[38] M. Sommariva, M. Catti, *Chemistry of Materials* **18**, 2411 (2006).

[39] M. Yashima, M. Itoh, Y. Inaguma, Y. Morii, *Journal of the American Chemical Society* **127**, 3491 (2005).

[40] Y. Inaguma, T. Katsumata, M. Itoh, Y. Morii, T. Tsurui, *Solid State Ionics* **177**, 3037 (2006).

[41] X. Gao, C. A. Fisher, T. Kimura, Y. H. Ikuhara, H. Moriwake, A. Kuwabara, H. Oki, T. Tojigamori, R. Huang, Y. Ikuhara, *Chemistry of Materials* **25**, 1607 (2013).

[42] Y. Inaguma, J. Yu, Y.-J. Shan, M. Itoh, T. Nakamuraa, *Journal of The Electrochemical Society* **142**, L8 (1995).

[43] T. Okumura, K. Yokoo, T. Fukutsuka, Y. Uchimoto, M. Saito, K. Amezawa, *Journal of Power Sources* **189**, 536 (2009).

[44] T. Okumura, T. Ina, Y. Orikasa, H. Arai, Y. Uchimoto, Z. Ogumi, *Journal of Materials Chemistry* **21**, 10061 (2011).

[45] Y. Inaguma, J. Yu, T. Katsumata, M. Itoh, *Journal of the Ceramic Society of Japan* **105**, 548 (1997).

[46] T. Tsurui, T. Katsumata, Y. Inaguma, *Solid State Ionics* **180**, 607 (2009).

[47] K. Kitaoka, H. Kozuka, T. Hashimoto, T. Yoko, *Journal of Materials Science* **32**, 2063 (1997).

[48] O. Maqueda, F. Sauvage, L. Laffont, M. Martínez-Sarrión, L. Mestres, E. Baudrin, *Thin Solid Films* **516**, 1651 (2008).

[49] S.-i. Furusawa, H. Tabuchi, T. Sugiyama, S. Tao, J. T. Irvine, *Solid State Ionics* **176**, 553 (2005).

[50] J.-K. Ahn, S.-G. Yoon, *Electrochemical and Solid-State Letters* **8**, A75 (2005).

[51] M. Morcrette, A. Gutierrez-Llorente, A. Laurent, J. Perrière, P. Barboux, J. Boilot, O. Raymond, T. Brousse, *Applied Physics A* **67**, 425 (1998).

[52] M. Morales, P. Laffez, D. Chateigner, I. Vickridge, *Thin Solid Films* **418**, 119 (2002).

[53] D. H. Kim, S. Imashuku, L. Wang, Y. Shao-Horn, C. A. Ross, *Journal of Crystal Growth* **372**, 9 (2013).

[54] T. Ohnishi, K. Takada, *Solid State Ionics* **228**, 80 (2012).

[55] K. Mitsuishi, T. Ohnishi, Y. Tanaka, K. Watanabe, I. Sakaguchi, N. Ishida, M. Takeguchi, T. Ohno, D. Fujita, K. Takada, *Applied Physics Letters* **101**, 073903 (2012).

[56] S. Kim, M. Hirayama, W. Cho, K. Kim, T. Kobayashi, R. Kaneko, K. Suzuki, R. Kanno, *CrystEngComm* **16**, 1044 (2014).

[57] S. Kim, M. Hirayama, K. Suzuki, R. Kanno, *Solid State Ionics* **262**, 578 (2014).

[58] R. Eason, *Pulsed Laser Deposition of Thin Films: Applications-Led Growth of Functional Materials* (John Wiley & Sons, 2007).

[59] A. Pimpinelli, J. Villain, *Physics of Crystal Growth*, vol. 53 (Cambridge university press Cambridge, 1998).

[60] J. Schou, *Applied Surface Science* **255**, 5191 (2009).

[61] K. Saenger, *Journal of Applied Physics* **70**, 5629 (1991).

[62] T. Ohnishi, B. Hang, X. Xu, M. Osada, K. Takada, *Journal of Materials Research* **25**, 1886 (2010).

[63] T. Ohnishi, K. Takada, *Applied Physics Express* **5**, 055502 (2012).

[64] J. M. Cowley, *Diffraction Physics* (Elsevier, 1995).

[65] B. D. Cullity, S. R. Stock, *Elements of X-ray Diffraction*, vol. 3 (Prentice hall Upper Saddle River, NJ, 2001).

[66] A. Ichimiya, P. I. Cohen, *Reflection High-Energy Electron Diffraction* (Cambridge University Press, 2004).

[67] F. J. Giessibl, *Reviews of Modern Physics* **75**, 949 (2003).

[68] J. Als-Nielsen, D. McMorrow, *Elements of Modern X-ray Physics* (John Wiley & Sons, 2011).

[69] P. Van der Heide, *X-ray Photoelectron Spectroscopy: An introduction to Principles and Practices* (John Wiley & Sons, 2011).

[70] G. L. Moore, *Introduction to inductively coupled plasma atomic emission spectrometry* (Elsevier, 2012).

[71] J. A. Van Loon, *Analytical Atomic Absorption Spectroscopy: Selected Methods* (Elsevier, 2012).

[72] E. Barsoukov, J. R. Macdonald, *Impedance Spectroscopy: Theory, Experiment and Applications* (John Wiley & Sons, 2005).

[73] J. Wei. Epitaxial growth of $Li_{3x}La_{2/3-x}TiO_3$ thin films on perovskite substrates by pulsed laser deposition (2012). Master Thesis.

[74] P. Zalm, *Journal of Vacuum Science & Technology B* **2**, 151 (1984).

[75] C. Kittel, *Introduction to Solid State Physics* (Wiley, 2005).

[76] Y.-H. Cho, J. Wolfenstine, E. Rangasamy, H. Kim, H. Choe, J. Sakamoto, *Journal of Materials Science* **47**, 5970 (2012).

[77] J. Dho, N. Hur, I. Kim, Y. Park, *Journal of Applied Physics* **94**, 7670 (2003).

[78] S. Chambers, M. Engelhard, V. Shutthanandan, Z. Zhu, T. Droubay, L. Qiao, P. Sushko, T. Feng, H. Lee, T. Gustafsson, E. Garfunkel, A. Shah, J.-M. Zuo, Q. Ramasse, *Surface Science Reports* **65**, 317 (2010).

[79] A. Shah, Q. Ramasse, S. May, J. Kavich, J. Wen, X. Zhai, J. Eckstein, J. Freeland, A. Bhattacharya, J. Zuo, *Physical Review B* **82**, 115112 (2010).